TOPICAL REVIEW — Magnetism, magnetic materials, and interdisciplinary research

Anisotropic nanocomposite soft/hard multilayer magnets*

Wei Liu(刘伟) and Zhidong Zhang(张志东)†

Shenyang National Laboratory for Materials Science, Institute of Metal Research, Chinese Academy of Sciences, Shenyang 110016, *China*

(Received 23 August 2017; published online 30 September 2017)

Experimental and theoretical researches on nanostructured exchange coupled magnets have been carried out since about 1988. Here, we review the structure and magnetic properties of the anisotropic nanocomposite soft/hard multilayer magnets including some new results and phenomena from an experimental point of view. According to the different component of the oriented hard phase in the nanocomposite soft/hard multilayer magnets, three types of magnets will be discussed: 1) anisotropic $Nd_2Fe_{14}B$ based nanocomposite multilayer magnets, 2) anisotropic $SmCo_5$ based nanocomposite multilayer magnets, and 3) anisotropic rare-earth free based nanocomposite multilayer magnets. For each of them, the formation of the oriented hard phase, exchange coupling, coercivity mechanism, and magnetic properties of the corresponding anisotropic nanocomposite multilayer magnets are briefly reviewed, and then the prospect of realization of bulk magnets on new results of anisotropic nanocomposite multilayer magnets will be carried out.

Keywords: anisotropic multilayer magnets, exchange coupling, effective interaction length, coercivity mechanism

PACS: 75.50.Bb **DOI:** 10.1088/1674-1056/26/11/117502

1. Introduction

Exchange couplings in magnetic thin films have attracted a great deal of attention in the areas of permanent magnets, magnetic recording, sensors, and spin electronics. The exchange-coupled permanent magnets are one of the model systems for studying the exchange couplings in magnetic thin films. The exchange-coupled magnets were firstly experimentally realized in ribbons by melt-spinning in 1988.[1] The merits of such magnets were a high saturation magnetization provided by a soft-magnetic phase and a mediate coercivity provided by a hard-magnetic phase if the two phases can be exchange-coupled well. Consequently, Kneller and Hawig[2] theoretically predicted a high maximum magnetic energy product and an unusually high remanence ratio or reduced remanence M_r/M_s, due to exchange coupling between nano-grains of the soft and hard magnetic phases. In addition, they predicted a unique magnetic behavior characterized by a reversible demagnetization curve, that is, a maximum recoil permeability as distinguished from the conventional single-phase permanent magnets, where the demagnetization curves reflect essentially the distribution of the irreversible switching fields. It is for this unique magnetic behavior of the nanocomposites, in a sense resembling a mechanical spring, that such magnets have been termed exchange-spring magnets by Kneller and Hawig. Skomski and Coey[3] attempted to predict the nucleation-field coercivities $H_c = H_N$ for three-dimensional two-phase nanostructures, which gave rise to a quantitative analysis of the permanent-magnet performance of oriented two-phase nanostructures. They predicted that the maximum energy product in suitably nanostructured $Sm_2Fe_{17}N_3/Fe_{65}Co_{35}$ composites was as high as 1090 kJ/m^3. But the maximum energy products of the rare-earth nanocomposite magnets prepared by means of rapid quenching and mechanical alloying have been much lower than the theoretical expectation, due to difficulties in controlling the nanostructures.[4–7] Although the remanence enhancement effect has been observed due to effective exchange coupling between hard and soft phases in such a bulk hard/soft phase system, the squareness of the demagnetization curve of the samples was not good enough for obtaining a higher energy product than that of the single phase, in which the hard phase is isotropic. The higher maximum energy product $(BH)_{max}$ was possible if the particle size (or layer thickness) of the soft-magnetic phase did not exceed the domain thickness of the hard-magnetic phase. However, in bulk samples, it was not so easy to control the microstructure compared with thin films. So, many works have been done on multilayer films or nanostructured films with Nd–Fe–B, PtFe, SmFe or SmCo as the hard magnetic phase.[8–13] Later, based on the summary and analysis of previous work on nanostructured exchange-coupled magnets[14] and our work on exchange couplings in magnetic films,[15] it was realized that the higher energy product may be obtained in anisotropic exchange-coupled multilayer magnetic films.

However, it is difficult to prepare anisotropy nanocomposite permanent magnets due to the difficulties in control-

*Project supported by the State Key Project of Research and Development of China (Grant No. 2017YFA0206302), the National Nature Science Foundation of China (Grant Nos. 51590883, 51331006, and 51471167), and the Chinese Academy of Sciences (Grant No. KJZD-EW-M05-3).

†Corresponding author. E-mail: zdzhang@imr.ac.cn

© 2017 Chinese Physical Society and IOP Publishing Ltd

ling the formation and alignment of the hard phase and diffusion between the hard and soft phases. It is well known that the temperature of the formation of the hard phases such as $Nd_2Fe_{14}B$, $SmCo_5$, and FePt should be above their crystallization temperature, for example, 550 °C. In addition, if the oriented hard phase is obtained, the anisotropic film will be directly epitaxially grown on single crystal substrates at high temperatures or at low temperatures following subsequent annealing at higher temperatures. It is easy to realize an anisotropic film of a single hard phase layer by means of the preparation method mentioned above, but for a multilayer with hard and soft phases, the formation and alignment of the hard phase are easily destroyed by diffusion of the soft phase at high temperatures. In order to solve this problem, Cui *et al.* realized an anisotropic soft- and hard-magnetic (SM and HM) nanocomposite multilayer by inserting a non-magnetic spacer layer to prevent diffusion between the SM and HM layers.[16] Thus, the oriented hard phase is well coupled with the soft phase layer. It is found that the interactions between SM and HM layers can well work over a very long distance, which cannot be fully understood based on the theories mentioned above.[2,3] So it is important to make clear the long-ranged interactions mechanism to obtain a higher energy product.

In this review, according to the different component of the oriented hard-magnetic phase in the nanocomposite soft/hard multilayer magnets, three types of magnets will be studied: 1) anisotropic $Nd_2Fe_{14}B$ based nanocomposite multilayer magnets, 2) anisotropic $SmCo_5$ based nanocomposite multilayer magnets, and 3) anisotropic rare-earth free based nanocomposite multilayer magnets. For each of them, the formation of the oriented hard phase, exchange coupling, coercivity mechanism, and magnetic properties of the corresponding anisotropic nanocomposite multilayer magnets are briefly reviewed, and then the prospect of realization of bulk magnets on new results of anisotropic nanocomposite multilayer magnets will be carried out.

2. The anisotropic $Nd_2Fe_{14}B$ based nanocomposite multilayer magnets

Generally, to obtain the Nd–Fe–B/α-Fe multilayer film, an easy way is to deposit α-Fe onto the top of the Nd–Fe–B layer. A Mo (50 nm)/$Nd_{16}Fe_{71}B_{13}$ (800 nm)/Fe (11 nm)/$Nd_{16}Fe_{71}B_{13}$ (800 nm)/Mo (50 nm) trilayer film onto a heated Si substrate was fabricated. The XRD patterns of all textured films show that the (105) reflection has the highest intensity. Figure 1(a) shows the hysteresis loop of the trilayer film at 295 K.[16] The magnetization along the perpendicular direction starts to drop drastically at a positive external field. The results obtained perpendicular and parallel to the film plane are anisotropic. However, exchange-decoupling behavior appears clearly in the perpendicular direction. This indicates that, due to interdiffusion between soft- and hard-magnetic phases in the interface region, the width of the soft-magnetic region is larger than the critical correlation length L_{ex} so that the soft phase is not exchange-coupled with the hard phase.

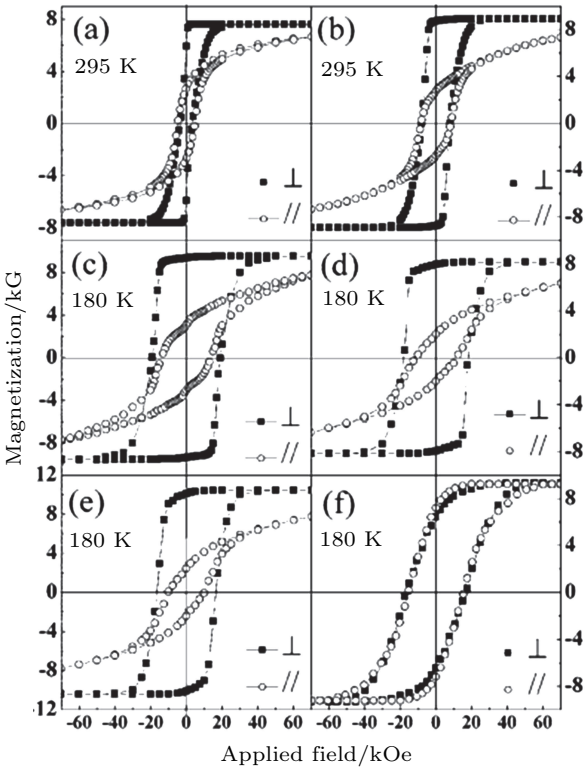


Fig. 1. Hysteresis loops of (a) the trilayer film Mo (50 nm)/$Nd_{16}Fe_{71}B_{13}$ (800 nm)/Fe (11 nm)/$Nd_{16}Fe_{71}B_{13}$ (800 nm)/Mo (50 nm) at 295 K, the textured multilayer film Mo (50 nm)/$Nd_{16}Fe_{71}B_{13}$ (800 nm)/Mo (2 nm)/Fe (11 nm)/Mo (2 nm)/ $Nd_{16}Fe_{71}B_{13}$ (800 nm)/Mo (50 nm) (b) at 295 K and (c) at 180 K, (d) the textured multilayer film Mo (50 nm)/ $Nd_{16}Fe_{71}B_{13}$ (800 nm)/Mo (4 nm)/$Nd_{16}Fe_{71}B_{13}$ (800 nm)/ Mo (50 nm) at 180 K, (e) the textured single-layered film Mo (50 nm)/$Nd_{16}Fe_{71}B_{13}$ (800 nm)/Mo (50 nm) at 180 K, (f) the isotropic multilayer film Mo (50 nm)/$Nd_{16}Fe_{71}B_{13}$ (800 nm)/Mo (2 nm)/Fe (11 nm)/Mo (2 nm)/$Nd_{16}Fe_{71}B_{13}$ (800 nm)/Mo (50 nm) at 180 K, with the magnetic field applied parallel (∥) and perpendicular (⊥) to the film plane.[16]

In order to prevent the interfacial diffusion, a Mo (2 nm) was deposited between the Fe layer and the Nd–Fe–B layer. A Mo (50 nm)/NdFeB (800 nm)/Mo (2 nm)/Fe (11 nm)/Mo (2 nm)/NdFeB (800 nm)/Mo (50 nm) multilayer film was prepared. The hysteresis loops measured at 295 K are shown in Fig. 1(b). Smooth loops can be observed along perpendicular and parallel directions. It can be seen that coercivity is increased from 4 kOe in Fig. 1(a) to 10 kOe with better squareness, indicating the good exchange-coupling between soft/hard magnetic phases. Such sandwiched microstructure can be proved by bright field and high-resolution transmission electron microscopy (HRTEM) images, as shown in Fig. 2. From Fig. 2(a), the columnar 2:14:1 grains are very clear. The Mo/Fe/Mo stack layer appears in between two Nd–Fe–B layers. In the HRTEM image, a bright line between the Nd–Fe–B layer and the Fe layer corresponds to the Mo spacer layer. This indicates that the soft/hard magnetic phases are well sep-

arated by the Mo spacer layer and interfacial diffusion is prevented. It means that by using the spacer layer, exchange-coupled hard/soft magnetic multilayer film with textured microstructure can be fabricated.

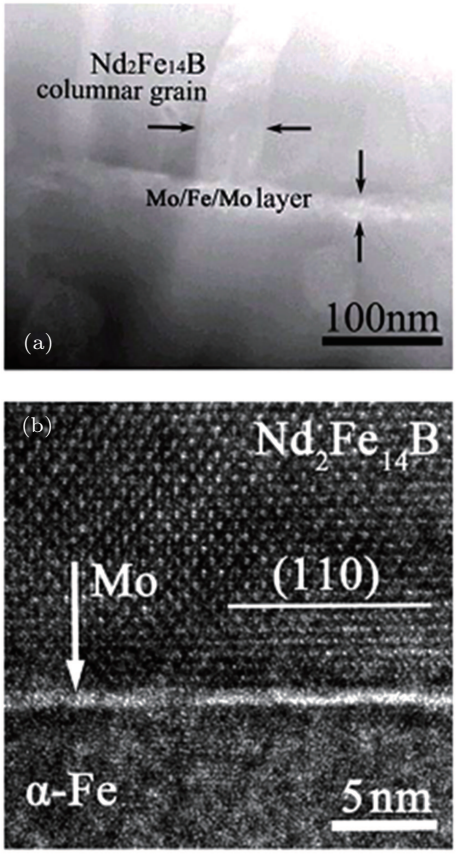


Fig. 2. Cross-sectional morphology image (a) and HRTEM image (b) at the interface region of the textured multilayer film Mo (50 nm)/$Nd_{16}Fe_{71}B_{13}$ (800 nm)/Mo (2 nm)/Fe (11 nm)/Mo (2 nm)/$Nd_{16}Fe_{71}B_{13}$ (800 nm)/Mo (50 nm).[16]

The hysteresis loops at 180 K of the textured Mo (50 nm)/$Nd_{16}Fe_{71}B_{13}$ (800 nm)/Mo (2 nm)/Fe (11 nm)/Mo (2 nm)/$Nd_{16}Fe_{71}B_{13}$ (800 nm)/Mo (50 nm) multilayer film are shown in Fig. 1(c). A good squareness of the demagnetization curve is observed in the direction perpendicular to the film plane. At 180 K, a clear kink in the hysteresis loop is found in the direction parallel to the film plane, which indicates exchange decoupling between hard and soft phases in the film. It is surprising that different exchange-coupling behavior is observed in the two measuring directions.

The thickness of the α-Fe layer has been changed to investigate its effect on the exchange-coupling between the soft/hard phases. Due to the existence of the Mo spacer layer, an effective critical correlation length L_{ex}^{eff} is proposed which is represented by the critical thickness of α-Fe at which a kink occurs in the demagnetization curve with increasing thickness of α-Fe. The effective critical correlation lengths at 295 K and 180 K in the two measuring directions are listed in Table 1. It is found that the effective critical correlation length is always smaller at 180 K than at 295 K, both perpendicular and parallel to the film plane. This temperature dependence is consistent with what is found in the isotropic case and is due to the enhanced magneto crystalline anisotropy at lower temperature. However, in the textured films, in contrast to the isotropic films, L_{ex}^{eff} is anisotropic and always larger in the perpendicular direction than in the parallel direction, both at 295 K and at 180 K. In order to confirm that the constricted shoulders originate from the exchange-decoupling between soft and hard phases due to the existence of the α-Fe layer, we prepared a textured trilayer film Mo (50 nm)/$Nd_{16}Fe_{71}B_{13}$ (800 nm)/Mo (4 nm)/$Nd_{16}Fe_{71}B_{13}$ (800 nm)/Mo (50 nm), in which the soft α-Fe layer is decreased to zero, and a textured single-layered film Mo (50 nm)/$Nd_{16}Fe_{71}B_{13}$ (800 nm)/Mo (50 nm) and measured their hysteresis loops at 180 K both parallel and perpendicular to the film plane (see Figs. 1(d) and 1(e)). It is clear that the demagnetization is smooth and that, in both directions, there are no kinks in the loop, confirming that the constricted shoulders are related with the α-Fe layer and indeed caused by exchange-decoupling between the soft and hard phases parallel to the film plane. Moreover, it is shown that there are no kinks as long as the thickness of the soft layer is below a critical value (see Table 1), which also proves that the exchange-decoupling is strongly related to the soft phase.

Table 1. Effective critical correlation length L_{ex}^{eff} for textured $Nd_2Fe_{14}B/\alpha$-Fe multilayer films in two directions at 295 K and 180 K.[16]

	295 K	180 K
L_{ex}^{eff} ($\perp$)	38 nm	26 nm
L_{ex}^{eff} ($\parallel$)	18 nm	10 nm

In comparison with the microstructure of the isotropic film, it is clear that the only difference is that the hard phase is of textured growth. Good squareness of hysteresis loops in the direction perpendicular to the film (the c-axis of the columnar grains) means that $N_\perp$ is close to 0 and $N_\parallel$ perpendicular to the c-axis of the columnar grains (in-plane direction of the film), is much larger than $N_\perp$. This is opposite to the case of isotropic multilayer films where $N_\perp$ is larger than $N_\parallel$. Therefore, it is easy to understand that additional shape anisotropy besides the magnetocrystalline anisotropy should be overcome when the demagnetization process is in the direction perpendicular to the c-axis of columnar grains (in-plane direction of the film) compared with the demagnetization along the c-axis of columnar grains (perpendicular to the film). To account for the shape anisotropy, a total effective anisotropy parallel to the film $\langle K_{eff}\rangle = \langle K_{mag}\rangle + \langle K_{shape}\rangle$ is proposed, where $\langle K_{mag}\rangle$ and $\langle K_{shape}\rangle$ represent the magnetocrystalline anisotropy and the shape anisotropy, respectively. Taking the shape anisotropy into consideration, we propose $L_{ex} = \pi(A/\langle K_{eff}\rangle)^{1/2}$, in accordance with Ref. [2].

When the effective critical correlation length L_{ex}^{eff} is measured in the parallel direction, it will be $\pi(A/(\langle K_{mag}\rangle+\langle K_{shape}\rangle))^{1/2}$, which is smaller than its value $\pi(A/K_{mag})^{1/2}$ in the perpendicular direction, both at low temperature and at room temperatures, as observed experimentally. Moreover, $\langle K_{mag}\rangle$ is larger at 180 K than at room temperature, which leads to a smaller L_{ex}^{eff} at 180 K than at room temperature for both directions, just like in the case of isotropic films. In order to prove what we propose above, we have measured the hysteresis loops at 180 K of an isotropic multilayer film Mo (50 nm)/$Nd_{16}Fe_{71}B_{13}$ (800 nm)/Mo (2 nm)/Fe (11 nm)/Mo (2 nm)/$Nd_{16}Fe_{71}B_{13}$ (800 nm)/Mo (50 nm) (Fig. 1(f)). Because the grains of the hard phase are isotropic in the film, the film shape leads to a slight difference between the two measuring directions. However, no kinks are observed in both directions, showing that the anisotropic correlation length found in the textured exchange-coupled hard/soft films is really due to the shape anisotropy of the textured structure of the hard phase.[16]

Cui *et al.* reported the structure, magnetic properties, and coercivity mechanism in textured $Nd_2Fe_{14}B/\alpha$-Fe multilayer films with Mo spacer layer.[17] Columnar $Nd_2Fe_{14}B$ grains grow along the direction perpendicular to the film's plane and the sandwich structure is preserved after deposition. Coercivity and rectangular ratio increase with decreasing temperature. It is concluded that reversal domain nucleation is the dominant mechanism in films. With increasing period number, the controlled coercivity mechanism is changed to the domain-wall pinning mechanism. The calculated width for planar inhomogeneities, thinner than domain wall thickness, increases with more periods. The coercivity analysis shows that the exchange-coupling of the hard/soft phase is not influenced by the existence of Mo spacer layer, which is confirmed by micromagnetic calculations for all five films.

From the above experiments, it is worth noticing that even when there are several nanometers of spacer layers the exchange-coupling between soft-magnetic and hard-magnetic phases can still happen. As mentioned above, once there are spacer layers between soft/hard magnetic layers, the structure would be like FM/NM/FM[18] trilayer or FM/NM/AFM[19] exchange bias systems. In the latter two cases, the NM spacer layer plays an important role in mediating the interlayer exchange coupling.

The strength of the exchange-coupling between soft/hard-magnetic layers is related to L_{ex}^{eff}. Due to the similarity in the film structure with those of FM/NM/FM[18] trilayer or FM/NM/AFM[19] exchangebias systems, it is interesting to investigate how the spacer layer affects the exchange coupling in hard-magnetic-layer/spacer-layer/soft-magnetic-layer systems. So, in the following part, some factors that influence the exchange-coupling are discussed.[20]

As can be seen in Fig. 1, it is clear that L_{ex}^{eff} shows an anisotropic behavior in textured multilayer films. By gradually increasing the thickness of the Fe layer, the L_{ex}^{eff} along directions perpendicular or parallel to the thin film plane measured at 295 K or 180 K can be obtained for a certain thickness of spacer layer. The inset in Fig. 3 shows an XRD pattern which is typical of all multilayer films with spacer layers. It can be seen that the intensity of the (105) reflection is largely enhanced, indicating the structure of strong *c*-axis textured films. In Fig. 3, the dependence of L_{ex}^{eff} on the thickness of the Mo spacer layer is shown, which was measured at 180 K and 295 K with the field applied either perpendicular or parallel to the film plane. Because L_{ex}^{eff} (180 K, $\|$) is very small and rapidly decreases to zero, its dependence on the thickness of Mo spacer layer is not obvious and shown in Fig. 3. L_{ex}^{eff} (295 K, $\perp$), which means L_{ex}^{eff} is measured at 295 K along the direction perpendicular to the thin film plane, decreases with increasing thickness of the Mo spacer layer, but does not vary significantly when the thickness of the Mo spacer layer varies between 4 nm and 6 nm. When the thickness of the spacer layer exceeds 8 nm, the L_{ex}^{eff} (295 K, $\perp$) decreases rapidly to zero. For the same thickness of spacer layer, the value of L_{ex}^{eff} (180 K, $\perp$) becomes smaller in comparison with that at room temperature, due to the enhanced magnetocrystalline anisotropy. In addition, the value of L_{ex}^{eff} (295 K, $\|$) is also smaller than L_{ex}^{eff} (295 K, $\perp$) under the same thickness of spacer layer, due to the contribution of the shape anisotropy of textured hard-magnetic phases. However, the nonlinear dependence of L_{ex}^{eff} (295 K, $\|$) or L_{ex}^{eff} (180 K,$\perp$) on the spacer-layer thickness is similar with that of L_{ex}^{eff} (295 K, $\perp$). Only a vertical shift along the *y* axis is observed due to the anisotropy.[2]

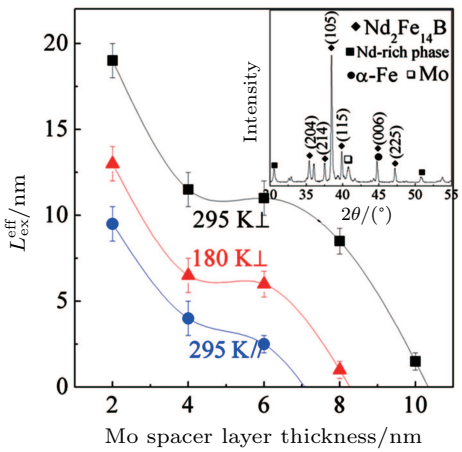


Fig. 3. (color online) Dependences of on the thickness of the Mo spacer-layer in Mo (50 nm)/NdFeB (800 nm)/Mo (*x* nm)/Fe (*y* nm)/Mo (*x* nm)/NdFeB (800 nm)/Mo (50 nm) multilayer films, measured at 180 K and 295 K with the applied field perpendicular and parallel to the film plane. The inset in Fig. 1(a) shows an XRD pattern typical of a textured HM/NM/Fe/NM/HM multilayer film.[20]

In order to identify whether such nonlinear dependence is spacer-layer dependent, Cu and Cr spacer layers were used.

Figure 4 shows the dependence of L_{ex}^{eff} (295 K, $\perp$) on the thickness of spacer layers (Cu or Cr) in NdFeB/α-Fe and Mo in PrFeB/α-Fe multilayers. Those dependences are qualitatively similar to that of L_{ex}^{eff} (295 K, $\perp$) as shown in Fig. 3, where a flat region can be seen between the thickness of the spacer layer from 4 nm to 8 nm, indicating that such nonlinear dependence is not sensitive to what materials are chosen for the NM spacer layer or hard-magnetic phases. But at the same thickness of spacer layer, the value of L_{ex}^{eff} is dependent on the spacer layer materials. From Fig. 4, when the thickness of spacer layer is thinner than 10 nm, the value of L_{ex}^{eff} for Cu as the spacer layer is larger than the value of L_{ex}^{eff} for Cr as spacer layer, which may be due to the intrinsic properties of spacer materials. When the thickness of the α-Fe layer is extrapolated to zero, this thickness of spacer layer is defined to be the decay length, indicating the depth that the soft-/hard-magnetic exchange coupling can propagate in the spacer layer. As seen from Fig. 4, for the cases of Cu spacer layer (curve a) and Cr spacer layer (curve b), the penetration length is around 11 nm. Since the dependence of L_{ex}^{eff} on the thickness of NM spacer layer is plotted along the direction perpendicular to the thin film plane at room temperature, compared with the penetration depth of around 11 nm in thin film with Mo as spacer layer materials (dark-square curve of Fig. 3), the penetration depth is not changed for different spacer layer materials. However, penetration depth is a temperature and texture-direction dependent parameter because it is reduced at lower temperature (triangle red curve in Fig. 3) or along the direction parallel to the thin film (blue circle curve in Fig. 3) due to the enhanced magnetocrystalline anisotropy at low temperature or the contribution of shape anisotropy in textured structure. When the hard-magnetic layer is changed into a Pr–Fe–B layer with Mo as spacer layer, the penetration length is also around 11 nm (curve c of Fig. 4). However, it is worth noting that the exchange-coupling between the soft- and hard-magnetic layers even happens when the thickness of the spacer-layer is as large as 10 nm, much larger than the decay length of 5 nm reported in exchange-biased AF/NM/FM trilayers.[19] Compared with the thickness of NM spacer layer in FM/NM/FM multilayer films,[18] it is concluded that the exchange coupling between the soft- and hard-magnetic phases is a long-ranged interaction.

Usually, the Hankel plot[21] is used to clarify the exchange-coupling or the static interaction between neighbor grains in hard magnets or hard/soft composites. The Hankel plot relates the isothermal remanence ratio $m_r(H)$ $(= M_r(H)/M_r(\infty))$, obtained through progressive magnetization, with demagnetization remanence ratio $m_d(H)$ $(= M_d(H)/M_r(\infty))$, obtained through progressive demagnetization from a previously saturated state to the same demagnetization field, where $M_r(\infty)$ is the remanence obtained in the saturated state. It is expressed as $\delta m(H) = m_d(H) - [1 - 2m_r(H)]$.[21] Figure 5 shows the typical Hankel plots of Mo (50 nm)/NdFeB (800 nm)/Cu (6 nm)/Fe (22 nm)/Cu (6 nm)/NdFeB (800 nm)/Mo (50 nm) and Mo (50 nm)/NdFeB (800 nm)/Cr (6 nm)/Fe (21 nm)/Cr (6 nm)/NdFeB (800 nm)/Mo (50 nm) thin film, in which the thickness of α-Fe is the L_{ex}^{eff} for a spacer layer of Cu (6 nm) and Cr(6 nm). The coercivities are also marked. Since the $\delta m(H)$ value is always negative for such two films in Fig. 5, it is proposed that there is at least the existence of magnetostatic interactions between soft- and hard-magnetic layers, which leads to the observed non-linear dependence.

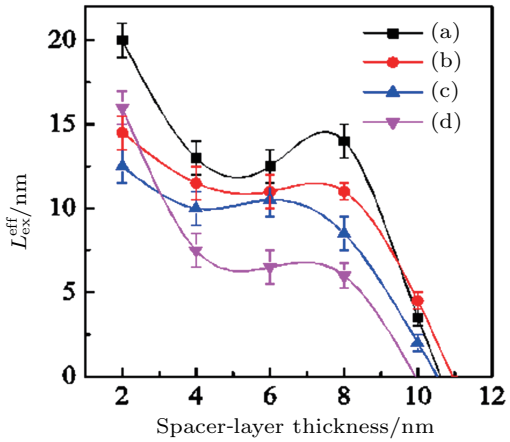


Fig. 4. (color online) L_{ex}^{eff} in Mo (50 nm)/*HM* (z nm)/*NM* (x nm)/Fe (y nm)/*NM* (x nm)/*HM* (z nm)/Mo (50 nm) (*NM* = Mo, Cu, or Cr, and *HM* = $Nd_{16}Fe_{71}B_{13}$ or $Pr_{16}Fe_{71}B_{13}$) multilayer films at 295 K, with the applied field perpendicular to the film plane. Its dependence on (a) *NM* = Cu for *HM* = $Nd_{16}Fe_{71}B_{13}$ (800 nm); (b) *NM* = Cr for *HM* = $Nd_{16}Fe_{71}B_{13}$ (800 nm); (c) *NM* = Mo for $Pr_{16}Fe_{71}B_{13}$ (800 nm) and (d) Mo for *HM* = $Nd_{16}Fe_{71}B_{13}$ (200 nm).[20]

Later, Cui *et al.*[22] realized anisotropic hard/soft multilayer films [Nd–Fe–B (30 nm)/Nd (3 nm)/Ta (1 nm)/$Fe_{67}Co_{33}$ (10 nm)/Ta (1 nm)]$_N$/Nd–Fe–B (30 nm)/Nd (3 nm) multilayer films (N = 0, 4, 9, 14,19) the Nd–Fe–B and Nd layers were each deposited at 600 °C. After the substrates were cooled down, the Ta (1 nm)/$Fe_{67}Co_{33}$ (10 nm)/Ta (1 nm) layers were deposited at around 200 °C. After depositing a stack of the Nd–Fe–B (30 nm)/Nd (3 nm)/Ta (1 nm)/$Fe_{67}Co_{33}$ (10 nm)/Ta (1 nm) layers, the substrate temperature was increased to 600 °C before depositing the next stack. After depositing all of these stacks, the thin films were annealed at 650 °C to allow Nd to diffuse into the Nd–Fe–B layer along the grain boundaries.

Based on the previous work mentioned above, the Ta spacer layer was found to be indispensible in keeping a high coercivity in $Nd_2Fe_{14}B$/Fe nanocomposite films. To attain a higher saturation magnetization in the nanocomposite films, a $Fe_{67}Co_{33}$ (10 nm) soft magnetic layer is used instead of the Fe layer since it has a higher saturation magnetization ($\mu_0 M_s$ = 2.35 T). In addition, the thickness of the Nd–Fe–

B layer is reduced to 30 nm to increase the volume fraction of the $Fe_{67}Co_{33}$ soft-magnetic phase. The Ta (1 nm) spacer layers are inserted to control the exchange coupling between the Nd–Fe–B/$Fe_{67}Co_{33}$ layers and to prevent interfacial reaction. Thus, nanocomposite mutlilayer films of [Nd–Fe–B (30 nm)/Nd (3 nm)/Ta(1 nm)/$Fe_{67}Co_{33}$ (10 nm)/Ta (1 nm)]$_N$/Nd–Fe–B (30 nm)/Nd (3 nm) were fabricated and the volume fraction of the soft magnetic phase was adjusted by the stack number N. Nd (3 nm) was used to enhance the coercivity of the Nd–Fe–B layers by the grain boundary diffusion. The hysteresis loops of the multilayer composite thin films with different N are shown in Fig. 6.[22]

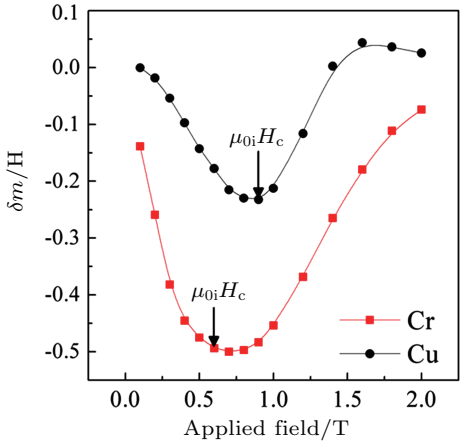


Fig. 5. (color online) Variation of $\delta m(H)$ as the function of applied field for the thin film Mo (50 nm)/NdFeB (800 nm)/Cu (6 nm)/Fe (22 nm)/Cu (6 nm)/NdFeB (800 nm)/Mo (50 nm) (dark) and Mo (50 nm)/NdFeB (800 nm)/Cr (6 nm)/Fe (21 nm)/Cr (6 nm)/NdFeB (800 nm)/Mo (50 nm) (red) measured along the direction perpendicular to the film plane.[20]

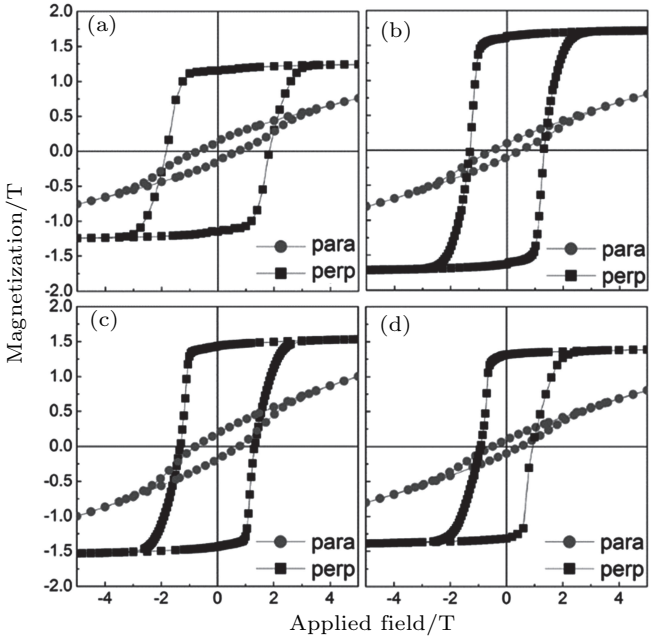


Fig. 6. Hysteresis loops of multilayer films Ta (50 nm)/[Nd–Fe–B (30nm)/Nd (3 nm)/Ta (1 nm)/Fe_2Co (10 nm)/Ta (1 nm)]$_N$/Nd–Fe–B (30 nm)/Nd (3 nm)/Ta (20 nm): (a) $N = 4$, (b) $N = 9$, (c) $N = 14$, and (d) $N = 19$.[22]

All the films show strong perpendicular anisotropy because of the preferred orientation of (001) planes parallel to the films. The remanent magnetization $\mu_0 M_r$ and maximum energy product $(BH)_{max}$ are shown in Fig. 7[22] as a function of the stack number N, together with the expected values from the film structures. The coercivity $\mu_0 H_c \approx 3$ T was realized in thin films with $N = 0$. It decreased monotonously to 1.77 T for $N = 4$ and 1.38 T at $N = 9$ due to the increased fraction of the $Fe_{67}Co_{33}$ soft magnetic phase. These coercivity values are higher than the typical ones for Nd–Fe–B sintered magnets ($\mu_0 H_c \approx 1.2$ T) because of the Nd diffusion process which weakened intergranular exchange coupling within the Nd–Fe–B layers. The lowest coercivity of 0.9 T is obtained for $N = 19$. The remanence (shown in Fig. 7b) increases gradually from 1.15 T for $N = 0$ to 1.25 T for $N = 4$. The remanence reaches the maximum value of 1.61 ± 0.05 T in the thin film with $N = 9$ and then decreases to $\mu_0 M_r = 1.54$ T for $N = 14$ and $\mu_0 M_r = 1.4$ T for $N = 19$. The initial increase in the remanence is due to the increasing volume fraction of the soft magnetic phase from zero for $N = 0$ to about 20% for $N = 19$. Correspondingly, the $(BH)_{max}$ (Fig. 7(c)) increases from 255 kJ·m^{-3} for $N = 0$ to 311 kJ·m^{-3} for $N = 4$. The highest $(BH)_{max}$ of 486 ± 15 kJ·m^{-3} is obtained in the thin film with $N = 9$. In the thin film with $N = 9$, experimentally measured $\mu_0 M_r = 1.61 \pm 0.05$ T is slightly higher than the designed value. It may be because the actual thickness of the film was thinner than the designed value due to the experimental error based on the predetermined sputtering rates of each layer. However, the experimental $(BH)_{max}$ is still lower than the designed one because the squareness of the actual demagnetization curve is not perfect. The $(BH)_{max}$ of ≈ 480 kJ·m^{-3} for $N = 9$ film is even comparable with the best performance

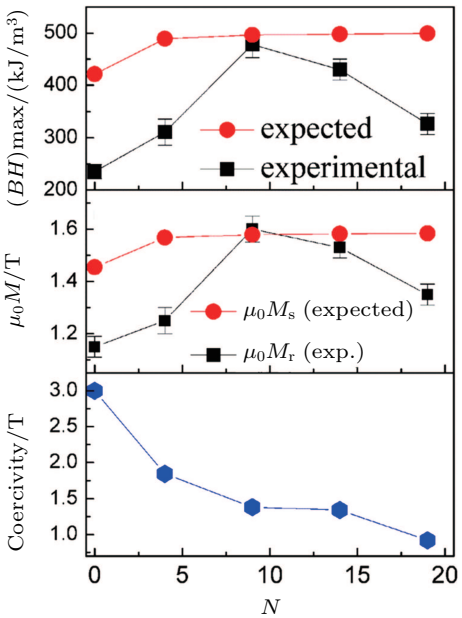


Fig. 7. (color online) Coercivity (a), remanence (b), and $(BH)_{max}$ (c) dependences of stack number N in multilayer films of Ta (50 nm)[Nd–Fe–B(30 nm)/Nd (3 nm)/Ta (1 nm)/$Fe_{67}Co_{33}$ (10 nm)/Ta (1 nm)]$_N$/Nd–Fe–B(30 nm)/Nd (3nm)/Ta (20 nm). The expected μM_s and theoretical $(BH)_{max}$ based on the expected μM_s are compared. The errors in the remanence and $(BH)_{max}$ are shown based on the errors on the thickness of the thin films.[22]

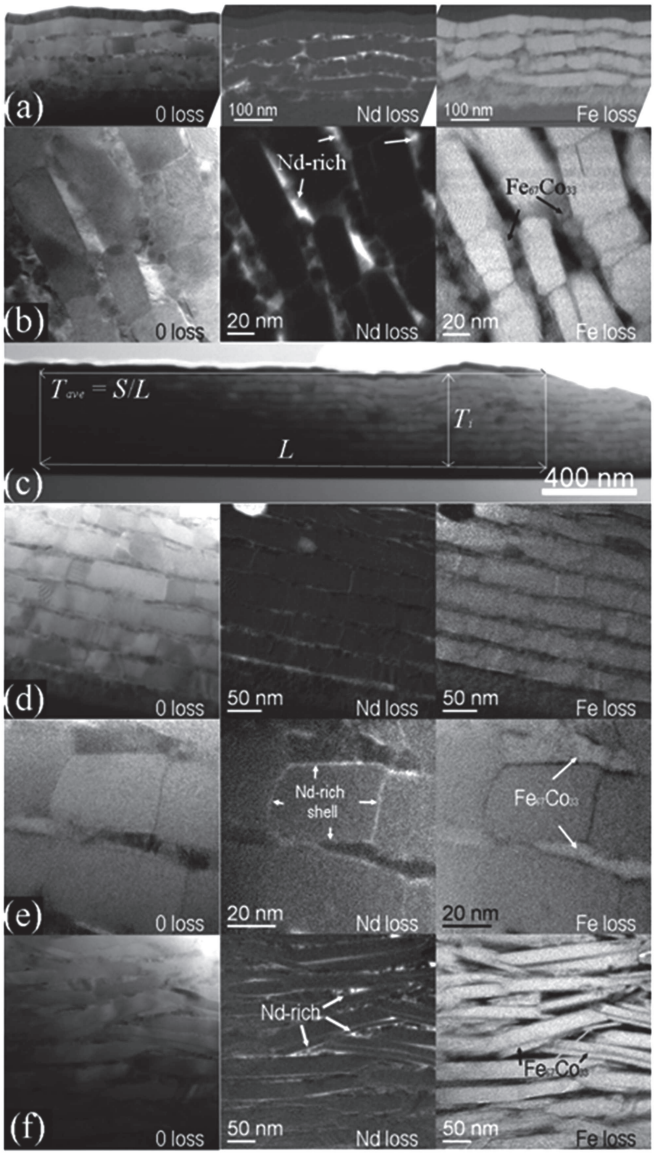


Fig. 8. Cross-sectional TEM images of multilayer films Ta (50 nm)[Nd–Fe–B (30 nm)/Nd (3 nm)/Ta (1 nm)/$Fe_{67}Co_{33}$(10 nm)/Ta (1 nm)]$_N$/Nd–Fe–B (30 nm)/Nd (3 nm)/Ta (20 nm) with stack numbers (a), (b) $N = 4$, (c)–(e) $N = 9$, and (f) $N = 14$.[22]

achieved in the strongly textured sintered magnet with a low fraction of the Nd-rich phase, 451 kJ·m^{-3}, which is the largest $(BH)_{max}$ ever achieved for anisotropic Nd–Fe–B composite films.[23]

The microstructures of these multilayer thin films are characterized by TEM as shown in Fig. 8.[22] Each layer can be clearly observed in the film with $N = 4$, Fig. 8(a). The corresponding Nd loss image shows that Nd is enriched in the interlayer region between the Nd–Fe–B layers. In the high-magnification TEM images in Fig. 8(b), $Nd_2Fe_{14}B$ grains are observed with rectangular crosssections and the *c*-axis normal to the film plane. These grains are closely packed within the Nd–Fe–B layer but separated by the Ta (1 nm)/$Fe_{67}Co_{33}$ (10 nm) Ta (1 nm) layers. The $Fe_{67}Co_{33}$ particles are embedded in the Nd-rich phase. It means that the Ta (1 nm)/$Fe_{67}Co_{33}$ (10 nm)Ta (1 nm) layers are fragmented during the growth at elevated temperature and $Fe_{67}Co_{33}$ are partially alloyed with Nd, causing a lower magnetization than the expected one. A low magnification cross sectional TEM image of the film with $N = 9$ is shown in Fig. 8(c) and is used to determine the average thickness. Figure 8(d) shows that Nd infiltrates into the interlayer region. In a higher magnification TEM image, Fig. 8(e), the $Nd_2Fe_{14}B$ grains have the same shape as that shown in Fig. 8(b). The Nd-rich phase forms a shell surrounding the $Nd_2Fe_{14}B$ grains, which is thought to be the reason for keeping the coercivity of the film ($\mu_0 H_c = 1.38$ T). However, the Nd-rich phase is not found to be alloyed with the $Fe_{67}Co_{33}$ phase as evidenced by the clear $Nd_2Fe_{14}B/Fe_{67}Co_{33}$ interfaces, thanks to the deposited Ta spacer layer. Figure 8(f) shows the TEM image of the thin film with $N = 14$. It shows the fragmented lamellae microstructure along the in-plane direction. The thick lamellae of about 30 nm and the thin lamellae of 10 nm correspond to the $Nd_2Fe_{14}B$ phase and the $Fe_{67}Co_{33}$ phase, respectively. The interlayer regions are enriched with Nd, similar to the Nd-rich phase distribution observed in the thin films with $N = 9$. Note that the $Nd_2Fe_{14}B$ phase grain shape in multilayer films ($N = 9$) is similar to that of hot pressed bulk nanocomposite magnets.[24]

To gain a better understanding of the coupling mechanism and demagnetization process in spacer-layer-tuned SM/HM multilayer systems, Cui *et al.* investigated the magnetic coupling mechanism between soft-/hard-magnetic (SM/HM) layers with various Ta and Fe thicknesses. Figure 9 compares the hysteresis loops of the NdFeB (100 nm)Nd (10 nm) SL film and those of the NdFeB (100 nm) Nd (10 nm)/Ta (*x* nm)/Fe (10 nm) films ($x = 0$, 2, 10, 50, 250, and 400).[25] In the SL film, good squareness and a high remanence ratio are achieved along the out-of-plane (OOP) direction, as shown in Fig. 9(a). Along the in-plane (IP) direction, the magnetization is hard to saturate, and a wide hysteresis is observed, indicating the strong perpendicular anisotropy. The coercivity of the SL film is ~1.2 T. When the Fe (10 nm) layer is deposited on the NdFeB film directly, the saturation magnetization is increased, while keeping the perpendicular anisotropy (Fig. 9(b)). However, owing to the exchange coupling between the NdFeB layer and the Fe layer, the coercivity is substantially decreased to 0.48 T, following the same tendency observed in Ref. [17]. When the Ta (2 nm) spacer layer was inserted between the SM and HM layers, the coercivity was recovered to 0.95 T, although not as high as 1.2 T of the SL film, owing to the existence of the Fe (10 nm) layer. Along the OOP direction, the magnetization starts to decrease from a positive field smoothly to the near-zero field. The squareness and remanence become lower compared with those of the SL film. In contrast, the discontinuity becomes observable along the IP direction, compared with the smoothness of near-zero fields along the OOP direction in

Figs. 9(a) and 9(b). The hysteresis loops of the films with Ta thickness from 10 nm to 250 nm can be seen in Figs. 9(c)–9(e). Along the OOP direction, a common feature is that the magnetization starts to decrease at a positive field with the smooth demagnetization process to the nucleation field of the HM layer. Along the IP direction, a kink is observed in all the Ta inserted films and becomes sharper with increasing thickness of the Ta spacer layer, indicating complete decoupling between SM/HM layers along the IP direction. When the thickness of Ta is further increased to 400 nm, a kink appears along the OOP direction. Note that the kink appears at 2 nm of the spacer layer along the IP direction, while it appears at 400 nm along the OOP direction. This indicates that the threshold thickness at which the kink appears is different along the OOP direction and the IP direction. Figure 9(h) shows the coercivity dependence on the thickness of the Ta spacer layer along the OOP direction. The coercivity of the films with a Ta spacer layer from 2 nm to 250 nm is between 0.8 T and 0.9 T, larger than 0.47 T for Ta-free film, but lower than 1.2 T for the SL film, owing to the existence of the SM layer. However, the coercivity is recovered to 1.34 T in the thin film with 400 nm thickness of Ta spacer. Because in this film the Fe moments are totally decoupled from the NdFeB layer and rotated easily by the external field, the rotation of Fe moments will not lead to the rotation of the moments in the NdFeB layer. Therefore, the coercivity of this film is dependent mainly on the NdFeB layer.

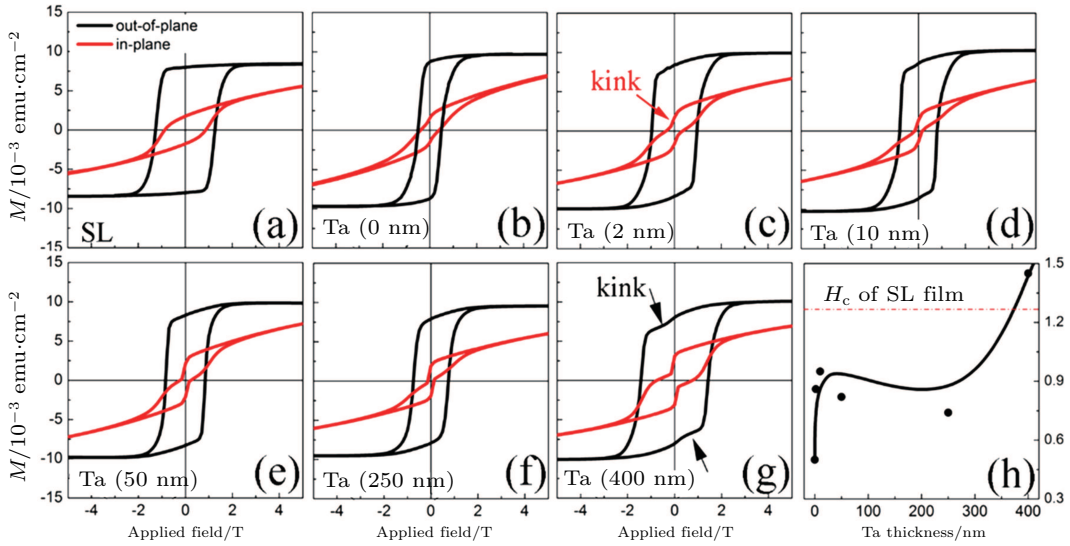


Fig. 9. (color online) Hysteresis loops of (a) Ti (20 nm)/NdFeB (100 nm)Nd (10 nm)/Ti (20 nm) SL film and (b)–(g) Ti (20 nm)/NdFeB (100 nm)Nd (10 nm)/Ta (x nm)/Fe (10 nm)/Ti (20 nm) nanocomposite films ((b) $x = 0$, (c) 2, (d) 10, (e) 50, (f) 250, and (g) 400). (h) The coercivity dependence of Ta thickness.[25]

Summarized from the hysteresis loops in Fig. 9, the change in the demagnetization process between near-zero field and the coercivity field for different thicknesses of Ta spacer layer is shown schematically in Fig. 10(a). Strong coupling leads to good squareness and higher remanence. In the saturated state, all the moments of Fe layer and NdFeB layer are parallel. At the nucleation field, some moments in the SM layer are already tilted from the OOP direction. Therefore, there will be a reduction in the saturation magnetization, termed as δM, as shown in Fig. 10(a). Figure 10(b) shows δM as a function of the thickness of Ta spacer layer. When the Ta spacer layer is thin, exchange coupling is dominant. Then, most of the Fe moments are pinned by the HM layer, leading to low δM. With thicker Ta, magnetostatic coupling becomes dominant, and some Fe moments rotate freely from the hard layer, leading to larger δM. It can be seen that, when the Ta spacer is thicker than 5 nm, dM is almost constant at 3×10^{-3} emu/cm^2, equal to twice the magnetization of Fe (10 nm) layers (see inset in Fig. 10(b)). This means that, once all Fe moments are reversed by the external field, magnetization reversal starts in the NdFeB layer. Therefore, between the zero field and the nucleation field, for each δM_i, the external field H_i is needed to rotate the moment from the remanence state to antiparallel alignment with NdFeB moments. So, the energy needed in this process is $\mathrm{d}\sigma = -H_i \mathrm{d}M_i$, which is numerically equal to the coupling energy of dM_i pinned by the HM layer. Therefore, the coupling energy along the OOP direction can be expressed as

$$\sigma = \sum \mathrm{d}\sigma i = -\int_{M_{\mathrm{NdFeB}}-M_{\mathrm{Fe}}}^{M_{\mathrm{r}}} H_i \mathrm{d}M_i,$$

where M_{r} is the remanence. M_{NdFeB}–M_{Fe} is the magnetization at nucleation field, at which state all Fe moments are almost antiparallel to the NdFeB moments. Here, σ includes the contributions from both exchange coupling and magnetostatic coupling, schematically represented by the area indicated in Fig. 10(c). Figure 10(d) shows the dependence of

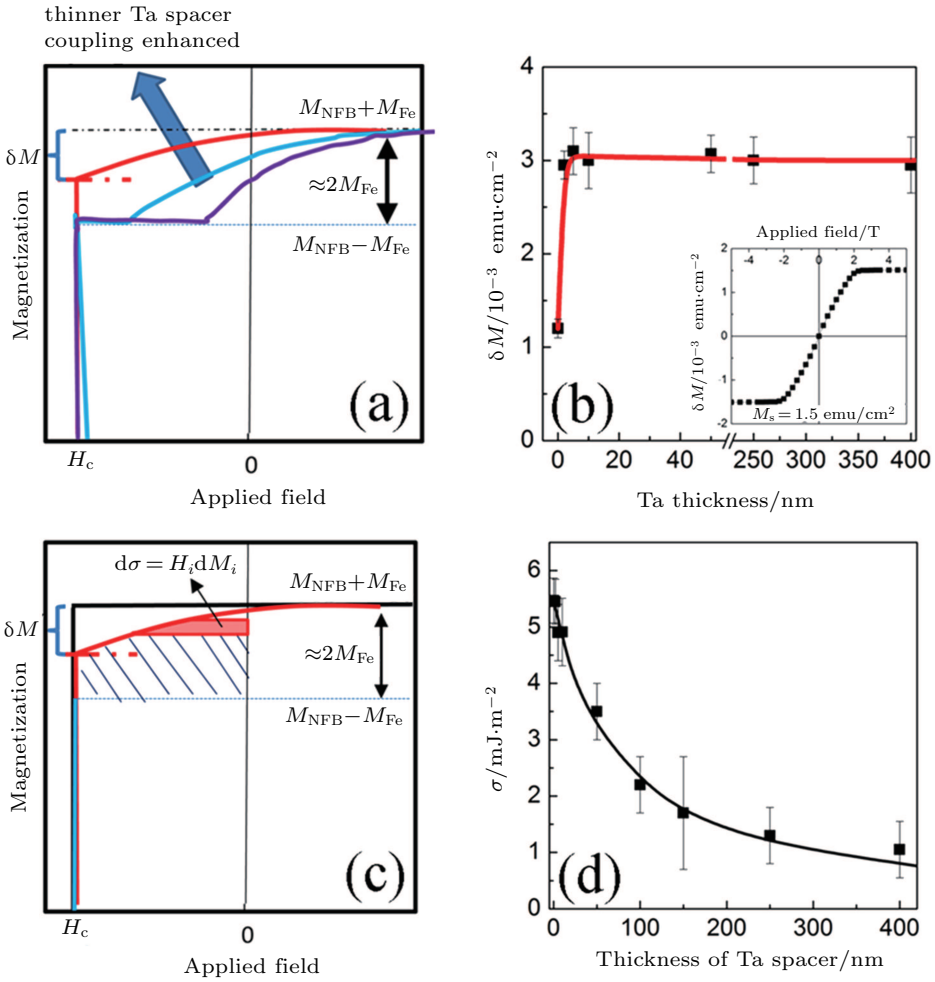


Fig. 10. (color online) (a) Schematics of the demagnetization process of thin films with different Ta thickness. (b) dM as a function of the thickness of Ta spacer layer in Ti (20 nm)/NdFeB (100 nm)Nd (10 nm)/Ta (x nm)/Fe (10 nm)/Ti (20 nm) films (x = 0–400). The inset shows the magnetization curve for 10 nm of the Fe layer. (c) Schematic of the estimation of coupling energy. (d) Coupling energy r as a function of the thickness of Ta spacer layer along the OOP direction.[25]

σ on the thickness of the Ta spacer layer along the OOP direction. When the Ta spacer is very thin, σ is ~ 5.5 mJ/m^2, which is comparable with 3–11 mJ/m^2 reported in Ref. [26] estimated by ferromagnetic resonance, indicating the reliability of this approach to estimate the coupling energy.

Figure 11 shows $(BH)_{max}$ as a function of the thickness of Ta in Ti (20 nm)/NdFeB (100 nm)Nd (10 nm)/Ta (x nm)/Fe (10 nm)/Ti (20 nm) films (x = 0–50) and the thickness of Fe in Ti (20 nm)/NdFeB (100 nm)Nd (10 nm)/Ta (2 nm)/Fe (y nm)/Ti (20 nm) films (y = 0–20). In Ti (20 nm)/NdFeB (100 nm)Nd (10 nm)/Ta (x nm)/Fe (10 nm)/Ti (20 nm) films, the initial increment of $(BH)_{max}$ from 113 kJ/m^3 in the film without Ta spacer to 205 kJ/m^3 in the film with 2 nm of Ta spacer is due to the recovery of coercivity as shown in Fig. 9. In Ti (20 nm)/NdFeB (100 nm)Nd (10 nm)/Ta (2 nm)/Fe (y nm)/Ti (20 nm) films, with increasing thickness of the Fe layer, the $(BH)_{max}$ increased from 195 kJ/m^3 at $y = 0$ to the maximum of 269 kJ/m^3 at $y = 5$. Ta and Fe layers that are too thick lead to either diluted magnetization or poor squareness and coercivity, causing a reduction in $(BH)_{max}$. It is noticed that the volume fraction of the SM phase in this model system is low. The squareness is also reduced by 2 nm in the Ta spacer layer and the free surface of the Fe layer. The highest $(BH)_{max}$ cannot be as high as the optimized $(BH)_{max}$ in a multilayer film.[22] Figure 11 indicates that strong exchange coupling is not indispensable in gaining higher $(BH)_{max}$ in agreement with the numerical simulation in Ref. [27]. By properly controlling the thickness of the Ta spacer layer and the SM layer, weakened exchange coupling can also lead to improved $(BH)_{max}$, assisted by magnetostatic coupling. A combination of weakened exchange coupling and magnetostatic coupling is promising for realizing superior $(BH)_{max}$ and moderate coercivity in anisotropy nanocomposites, as reported in multilayer systems.[22]

From the results mentioned above, it can be concluded that the interactions between soft- and hard-magnetic layers can still work well over a very long distance, which is several times larger than the Rudermann–Kittel–Kasuya–Yosida (RKKY) type of interaction reported in Fe/Cr/Fe multilayer film[27–29] and the Heisenberg exchange interaction. This kind of long-range interaction is a good supplementary for the exchange-coupling model of nanocomposite magnets.[3,30]

Thus, it is very important to make clear the mechanism of the long-range interactions between the hard- and soft-magnetic layers. Dai *et al.*[31] analyzed the interactions mechanism by using the first-order-reversal-curves (FORCs) distributions and discussed the dependence of the mean interaction on the distance between soft- and hard-magnetic layers.

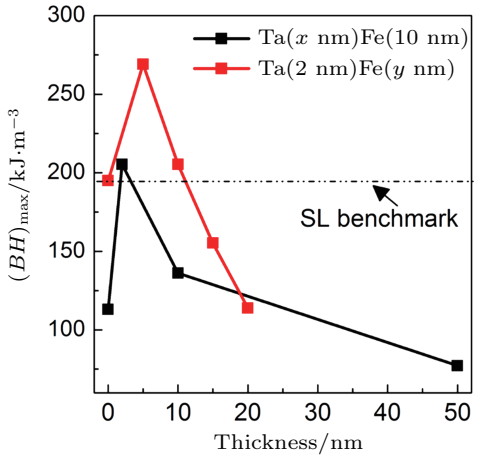


Fig. 11. (color online) $(BH)_{max}$ as a function of the thickness of the Ta spacer layer in Ti (20 nm)/NdFeB (100 nm)Nd (10 nm)/Ta (x nm)/Fe (10 nm)/Ti (20 nm) films (x = 0–50) and the thickness of Fe layer in Ti (20 nm)/NdFeB (100 nm)Nd (10 nm)/Ta (2 nm)/Fe (y nm)/Ti (20 nm) films (y = 0–20). The dashed line stands for the $(BH)_{max}$ benchmark of SLTi (20 nm)/NdFeB (100 nm)Nd (10 nm)/Ti (20 nm) thin film.[25]

The room-temperature in-plane (IP) and out-of-plane (OOP) hysteresis loops of Nd–Dy–Fe–Co–B (150 nm)/MgO (t_{MgO})/Fe (10 nm) (t_{MgO} = 0 nm, 2 nm, 60 nm, 70 nm, and 100 nm) multilayers are shown in Fig. 12. Along the OOP direction, the Nd–Dy–Fe–Co–B single layer (Fig. 12(a)) shows a coercivity of 23 kOe and a good squareness. When the soft-magnetic α-Fe layer is directly deposited on the Nd–Dy–Fe–Co–B layer (Fig. 12(b)), the remanence of the film increases in comparison with that of the Nd–Dy–Fe–Co–B single-layer due to the interactions between $Nd_2Fe_{14}B$ and soft-magnetic α-Fe. On the other hand, the coercivity decreases to 6 kOe due to interdiffusion in the interface region between the soft- and hard-magnetic layers. When the MgO (t_{MgO} = 2 nm) spacer layer is inserted, a coercivity of 19 kOe is obtained. The increased remanence and smooth hysteresis loop ranging from the positive saturation field to the nucleation field confirm that the soft- and hard-magnetic layers are well coupled through the MgO spacer layer. When t_{MgO} increases to 70 nm (see Fig. 12(e)), initially a kink appears in the OOP hysteresis loop of the film, due to the decoupling between the soft- and hard-magnetic layers. Upon further increase of t_{MgO} to 100 nm, a poor squareness with a substantial decrease of the remanence is found. Along the IP direction, a kink is observed in all MgO-inserted films which become sharper with increasing thickness of the MgO spacer layer. This anisotropic coupling behavior observed in the two measuring directions implies the existence of different effective correlation lengths due to different shaped anisotropies along the two directions.[16,22]

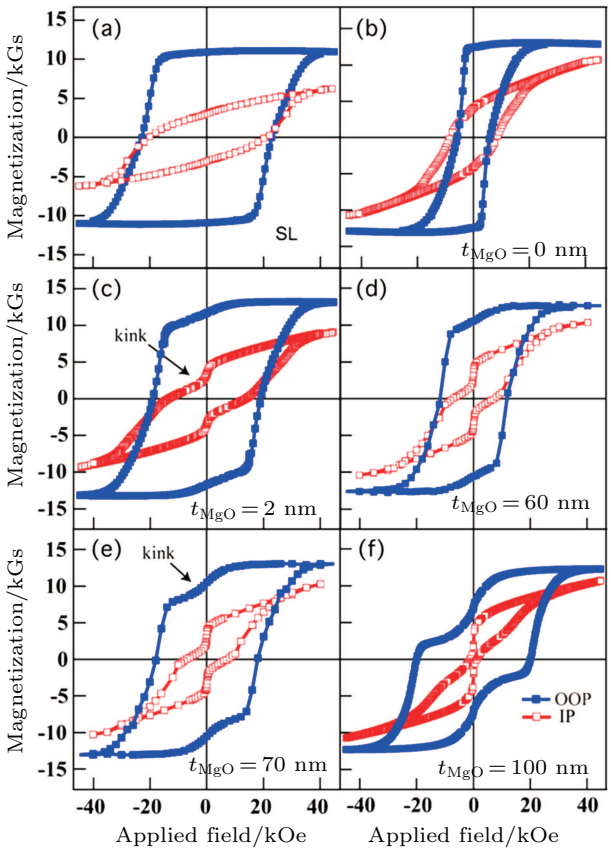


Fig. 12. (color online) The room temperature in-plane (IP) and out-of-plane (OOP) hysteresis loops of Nd–Dy–Fe–Co–B (150 nm)/MgO (t_{MgO})/Fe (10 nm) (t_{MgO} = 0 nm, 2 nm, 60 nm, 70 nm, and 100 nm).[31]

The OOP demagnetization curves of multilayers with Ta and Cr_2O_3 spacer layers are presented in Figs. 13(a) and 13(b), respectively. It is found that the effective interaction length (L^{eff}) is different for Ta, Cr_2O_3, and MgO spacer layers. Here, L^{eff} is defined as the thickness of the spacer layer at which the kink in the hysteresis loop initially appears, which is different from the definition in the previous work.[16] As can be seen in Figs. 13(a) and 13(b), the demagnetization curves indicate at which thickness of the spacer layer the kink appears. For the Ta spacer layer, L^{eff} = 150 nm, while, for the Cr_2O_3 spacer layer, L^{eff} = 20 nm. The exchange interactions propagated by itinerant electrons in metallic systems are well understood in terms of the RKKY type of interaction and will exponentially decrease by the insulating spacer layers due to electron tunneling in the limit of ultrathin spacer layers.[32,33] It is expected that the RKKY interaction and the dipolar interaction coexist in the multilayer with the metallic Ta spacer layer, while the insulating MgO and Cr_2O_3 spacer layers will eliminate the influence of the exchange interaction at the surface between the soft- and hard-magnetic layers. Accordingly, different values of L^{eff} are observed for the multilayers upon the use of different spacer-layer materials. It is clear that L^{eff} ($\approx$ 70 nm)

for the MgO spacer layer should be larger than L^{eff} for Cr_2O_3 ($\approx$ 20 nm) spacer layer. Since Cr_2O_3 is an antiferromagnet with blocking temperature T_B around 307 K, the smaller L^{eff} may result from the antiferromagnetic structure, which suppresses the interactions between the hard- and soft-magnetic layers.

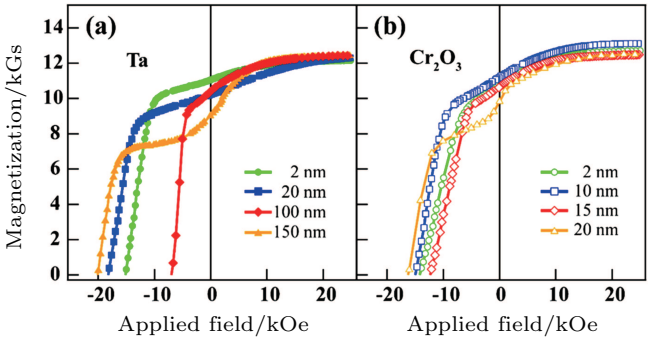


Fig. 13. (color online) OOP demagnetization curves of Nd–Dy–Fe–Co–B (100 nm)/S/Fe (10 nm). (a) The thicknesses of the Ta spacer layers are 2 nm, 20 nm, 100 nm, 150 nm and (b) the thicknesses of the Cr_2O_3 spacer layers are 2 nm, 10 nm, 15 nm, 20 nm.[31]

To understand the nature of long-range interactions in anisotropic nanocomposite multilayers, FORC diagrams are made. The FORC distributions are thought to be highly sensitive to the interacting particles and have been widely used on nanocomposite magnets.[34–37] It was initially proposed as a method to identify the Preisach model parameters and was later extended as a model-independent technique to characterized the hysteresis in the magnetization reversals of the magnetic materials.[38,39] Subsequently, it has been proven to be a useful technique to model the behavior of hysteretic materials, including the determination of interactions in multiphase magnetic systems.[40] The acquisition of a FORC begins by saturating the system in a positive applied field. Then the applied field is decreased to a reversal field H_r, and the magnetization M is measured starting from H_r back to positive saturation.[41,42] The magnetization on a FORC curve at an applied field H_a for a reversal field H_r is denoted by $M(H_a, H_r)$, where $H_a \geq H_r$. A FORC distribution is defined as[43,44]

$$\rho(H_r, H_a) = -\frac{1}{2}\frac{\partial^2 M(H_r, H_a)}{\partial H_r \partial H_a},$$

which eliminates the purely reversible components of the magnetization. Thus, any non-zero value corresponds to irreversible switching processes. The FORC distribution can also be represented in (H_c, H_b) coordinates, where H_c corresponds to the coercive field of each single-domain loop in the absence of interactions and H_b is the local interaction field, by means of a rotation of the coordinate system defined by $H_b = (H_a + H_r)/2$ and $H_c = (H_a - H_r)/2$.[39] Compared with other similar experimental methods, the FORC is more convenient because it does not require the magnetization to be measured in a remanent state or an AC demagnetized state. In addition, the FORC method gives more information than the ΔM curve including the information about coercivity distribution and the dependence of the ratio of the reversible and irreversible magnetization processes on the reversible field H_r.[42]

A number of color lines filling the interior of the major hysteresis loops of the Nd–Dy–Fe–Co–B single layer and the Nd–Dy–Fe–Co–B (100 nm)/Ta (2 nm)/Fe (10 nm) multilayer are shown in Figs. 14(a) and 14(c). The contour plots of the FORC distribution as a function of H_a and H_r are represented by three different horizontal dashed lines at H_r along H_a in Figs. 14(b) and 14(d) (the reference marks 1, 2, 3 are marked in Figs. 14(a) and 14(c)). For the Nd–Dy–Fe–Co–B single layer (Fig. 14(b)), the reversal is initiated by the formation of domain walls and their successive movements. This is indicated by marking 1 around -15 kOe. Generally, less energy is required for domain-wall motion compared to coherent rotation of the magnetization. So, after saturating the magnet, the domain wall starts moving during the reversal process from one energy minimum to another. In this process, after the Nd–Dy–Fe–Co–B film has initiated nucleation, the applied field will not bring the system back to the initial states, which gives rise to an irreversible magnetization when the applied field returns back. Thus, it can be concluded that the domain nucleation occurs around the field range from -15 kOe to -23 kOe (between line 1 and line 2) with a decrease of the magnetization in the major loop. Two non-zero tails of the FORC distribution are seen between lines 2 and 3 (-23 kOe$< H_r < -34$ kOe). The significance of irreversible processes is due to the onset of annihilation of the domains, which continues until negative saturation. Figure 14(d) shows the FORC distribution of the Nd–Dy–Fe–Co–B/Ta (2 nm)/Fe multilayer. Here, the beginning of irreversible switching is around line 1 at $H_r < 12$ kOe. Between lines 1 and 2 (-12 kOe$< H_r < -20.5$ kOe), the nucleation process happens as the domains of the soft-magnetic phase are pinned with the hard-magnetic phases which leads to irreversible switching of both the hard- and soft-magnetic phases. This corresponds to the fact that both the hard- and soft-magnetic layers are well coupled with each other. Non-zero tails of the FORC distribution are observed between lines 2 and 3 (-20.5 kOe $\langle H_r < -29$ kOe) accompanied with a number of negative areas below line 2 ($H_r < -20.5$ kOe). This indicates the onset of annihilation of the domains.

Combining the characteristics of the hysterons and the FORC distribution function,[40] the FORC diagrams of the multilayer system with a mean interaction field were obtained in Figs. 15(a)–15(e). In the FORC distribution of Nd–Dy–Fe–Co–B single layer (Fig. 15(a)), a peak ($\rho_{\max}$) with two branches (one along the $H_b = 0$ axis, another one in the negative H_b direction) forming a "wishbone" structure is shown. As the Fe layer is added (Fig. 15(b)), $\rho_{\max}$ increases initially.

With increasing the thickness of the inserted Ta spacer layer from 0 to 150 nm (Figs. 15(c)–15(e)), ρ_{max} continuously decreases. In principle, a larger value of ρ indicates a larger ferromagnetic interaction, which originates from the interactions between the soft- and hard-magnetic layers. From the phenomenon mentioned above, it can be concluded that, with increasing thickness of the spacer layer, the average interaction becomes weaker. Additionally, in Fig. 15(e), another peak (indicated by an arrow) appears in the low-H_c region. According to the phenomenon that a kink appears in the major hysteresis loop if the soft-magnetic and hard-magnetic layers become decoupled (Fig. 13(a)), it indicates that the low-H_c region originates from individual switching of the soft-magnetic layer in the multilayer. By observing the behavior of the maximum in the FORC distribution, one can conclude: For the Nd–Dy–Fe–Co–B single layer, the maximum of FORC distribution is centered around $H_b = 0$ kOe. By direct coupling with Fe, the value becomes $H_b = 1.5$ kOe. When the thickness of the spacer layer is 2 nm, the maximum of FORC distribution lies around $H_b = 1.6$ kOe. Upon further increasing the thickness to 100 nm, it reaches $H_b = 2.2$ kOe. Eventually, when $S_{Ta} = 150$ nm, the maximum of FORC lies around $H_b = 0$ kOe. According to the results reported by Pike *et al.*,[39] when a mean interacting field is introduced in an assembly of non-interacting single-domain particles, the maximum in the FORC distribution is generally located on the $H_b = 0$ axis. If the interaction is of a dipolar type, the distribution will go into a positive H_b direction, giving a maximum centered at a positive H_b. Meanwhile, the exchange interaction causes a negative shift of the FORC distribution, which leads to a negative H_b. In the Nd–Dy–Fe–Co–B single layer, the grains of the oriented $Nd_2Fe_{14}B$ phase are well separated by the grain-boundary phase and the exchange coupling between adjacent hard grains is weak. In the multilayer system with Fe layer, the mean interaction is dipolar in nature. However, upon increasing the thickness of the spacer layer to 150 nm, both the peaks at the high and low values of H_c are located at $H_b = 0$ kOe. This indicates that the interaction between the soft- and hard-magnetic layers is weak.

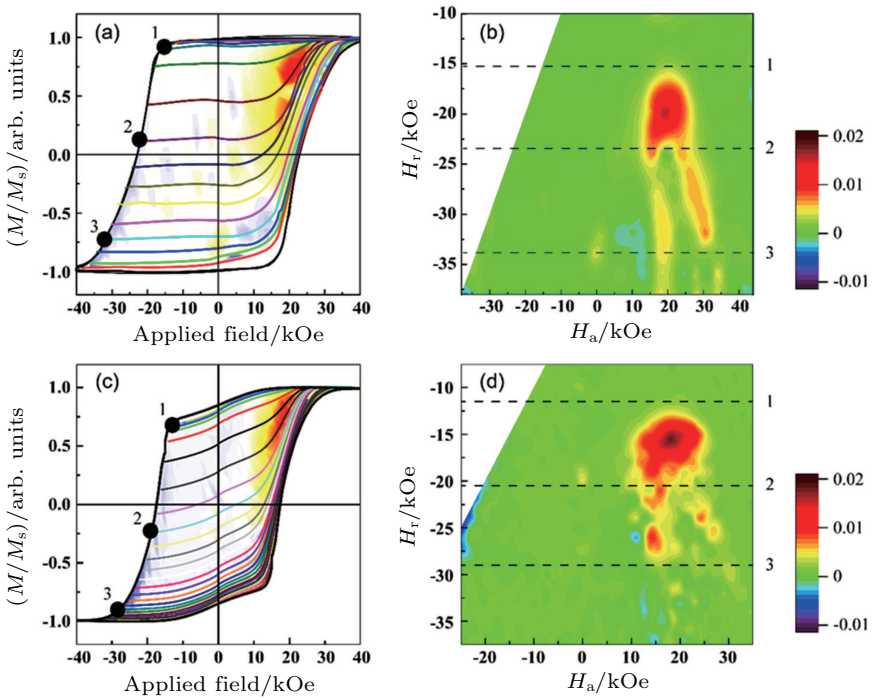


Fig. 14. (color online) (a) Color lines: first-order reversal curves for single-layer Nd–Dy–Fe–Co–B. Color contour plots: M and H_r dependence of the FORC function distribution; (b) the main analysis data: color contour plots of the H_c and H_b dependence of FORC function distribution. (c) Color lines: first-order reversal curves for Nd–Dy–Fe–Co–B (100 nm)/Ta (2 nm)/Fe (10 nm) multilayer. Color contour plots: M and H_r dependence of the FORC function distribution; (d) the main analysis data for Nd–Dy–Fe–Co–B (100 nm)/Ta (2 nm)/Fe (10 nm) multilayer: color contour plots of the H_c and H_b dependence of FORC function distribution. The color scale represents the distribution of the values of ρ.[31]

The quantitatively extracted reversible and irreversible components from the FORC diagrams of the Nd–Dy–Fe–Co–B single layer and Nd–Dy–Fe–Co–B (100 nm)/Ta/Fe (10 nm) multilayers are presented in Figs. 15(f) and 15(g). The separation of the reversible and irreversible processes has been carried out near the descending branch of the major loop by monitoring the magnetization change versus H_r in the original FORC. In mathematical form, the reversible/irreversible parts are represented by the following equations:[45,46]

$$\begin{aligned} \mathrm{d}M^{\mathrm{rev}}(H_r) &= \lim_{H_a \to H_r} [M(H_r, H_a) - M(H_r)], \\ \mathrm{d}M^{\mathrm{rr}}(H_r) &= \lim_{H_a \to H_r} [M(H_a) - M(H_r, H_a)], \\ \mathrm{d}M^{\mathrm{rev}}(H_r) &= \lim_{H_a \to H_r} [M(H_r, H_a) - M(H_r \mathrm{d}M^{\mathrm{rev}}(H_r))] \end{aligned}$$

$$= \lim_{H_a \to H_r} [M(H_r, H_a) - M(H_r dM^{rev}(H_r))]$$
$$= \lim_{H_a \to H_r} [M(H_r, H_a) - M(H_r)].$$

Integration of the dM/dH_r curves will quantitatively reflect the magnetic entities involved in the reversible or irreversible process. The soft-magnetic part in the magnet contributes mostly to the reversible components, whereas the hard-magnetic part requires the larger fields to rotate the irreversible components. Therefore, the maximum value of the irreversible process is around the coercive field (see Fig. 15(f)) and the maximum of the reversible process is around $H_r = 0$ kOe (see Fig. 15(g)). Since the percentage of hard-magnetic layer in the present experiments is approximately 90%, the switching mechanism of the multilayers is highly irreversible. By fitting the experimental irreversible and reversible values to Gauss distributions, the effective areas have been calculated. As a result, 99% of the area is associated with the irreversible magnetization of the Nd–Dy–Fe–Co–B single layer and 97%, 94%, 90%, and 64% with the irreversible magnetization of the Nd–Dy–Fe–Co–B (100 nm)/Ta/Fe (10 nm) multilayers with $S_{Ta} = 0$ nm, 2 nm, 100 nm, and 150 nm, respectively. Although, the ratios of soft- and hard-magnetic layers are fixed in the series of multilayers, the amount of the irreversible magnetization continuously decreases with increasing thickness of the spacer layer. This indicates that, with increasing thickness of the spacer layer, the shape anisotropy overcomes the weakened interactions between soft- and hard-magnetic layers and forces the magnetization into a reversible process.

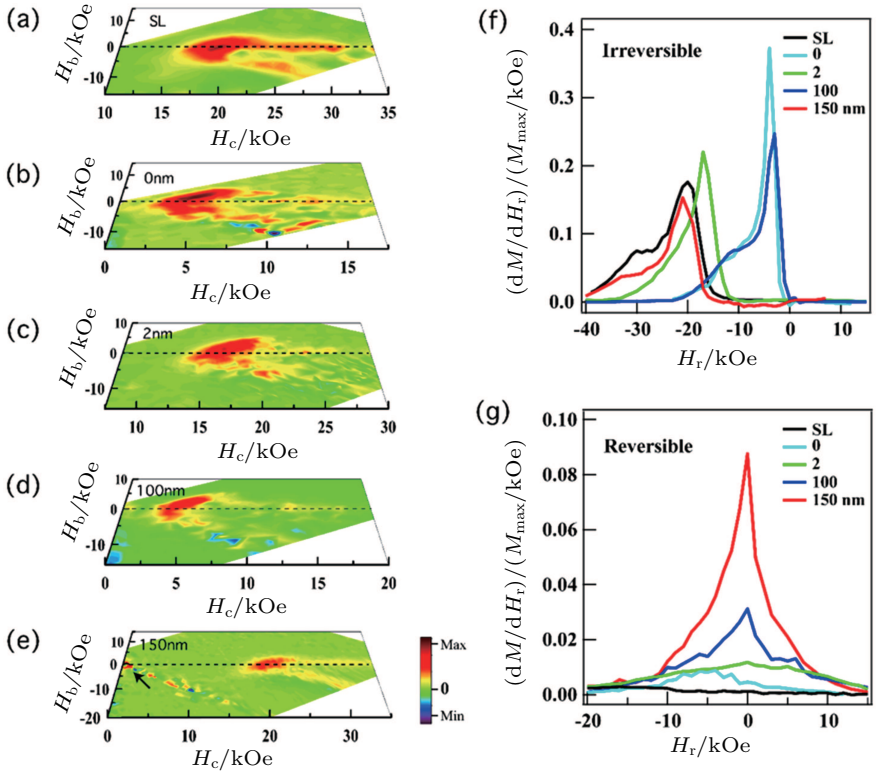


Fig. 15. (color online) Contour plot images converted from FORCs for (a) Nd–Dy–Fe–Co–B, (b) Nd–Dy–Fe–Co–B/Fe, (c) Nd–Dy–Fe–Co–B/Ta (2 nm)/Fe, (d) Nd–Dy–Fe–Co–B/Ta (100 nm)/Fe, and (e) Nd–Dy–Fe–Co–B/Ta (150 nm). Extracted (f) irreversible and (g) reversible distributions, which correspond to the samples in panels (a)–(e).[31]

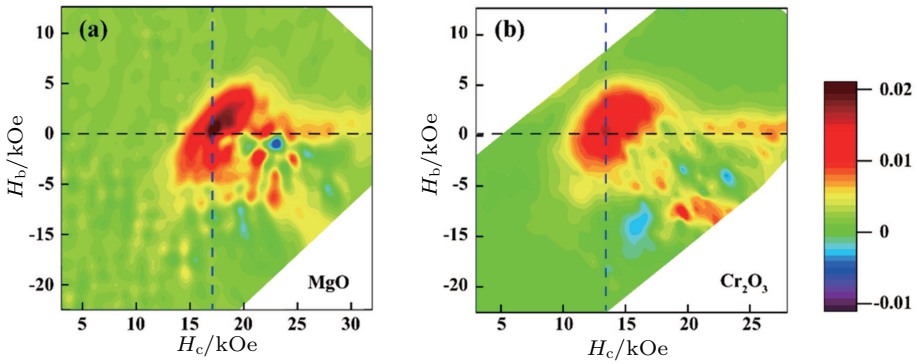


Fig. 16. (color online) (a) FORC distributions for Nd–Dy–Fe–Co–B/MgO (5 nm)/Fe in H_b vs. H_c representation. (b) FORC distributions for Nd–Dy–Fe–Co–B/Cr_2O_3 (5 nm)/Fe in H_b vs. H_c representation.[31]

The exchange-coupling between the hard- and soft-magnetic nanocomposite magnets based on the FORC method has been reported earlier.[34–37] When soft- and hard-magnetic layers are coupled with each other beyond a critical distance, the weak long-range dipolar interaction becomes dominant. According to the results of Cui *et al.*[25] and Gabay *et al.*,[47] the dipolar interaction may play an important role in combining the soft- and hard-magnetic phases. To investigate the FORC distribution of a multilayer with insulating spacer layer, the contour plots of the multilayers with MgO (5 nm) and Cr_2O_3 (5 nm) spacer layer are presented in Figs. 16(a) and 16(b), respectively, in which ρ_{max} is indicated by the blue dashed line. For the MgO spacer layer, ρ_{max} is 0.0223, which is nearly the same as for $S_{Ta} = 2$ nm (Fig. 15(c)), whereas for the Cr_2O_3 spacer layer, ρ_{max} is 0.0178. The lower ρ value for the film with the Cr_2O_3 spacer layer indicates a smaller ferromagnetic interaction because of the lower concentration of the ferromagnetic phases present in the system.[44] It indicates that an antiferromagnetic spacer layer can suppress the interactions between hard- and soft-magnetic layers. It can be seen from the interaction field distribution that ρ_{max} is localized around $H_b = 270$ Oe for MgO spacer layer, which is tilted towards positive H_b. Therefore, the mean interaction is of dipolar type in the multilayer with MgO spacer layer. For the Cr_2O_3 spacer layer, ρ_{max} is localized around $H_b = 28$ Oe, which indicates that the interactions between the hard- and soft-magnetic layers are weak. Regarding the distribution of the position of ρ_{max}, it can be concluded that the position of ρ_{max} along the H_b direction is not only associated with the thickness of the spacer layer but also with the materials of the spacer layer.

Nanocomposite multilayers, which are consist of independent soft- and hard-magnetic layers (SM/HM), present an advantage on controlling the competition of the surface- or interface-induced interactions. Therefore, it is desirable to further study the magnetic interactions via directly observing the domain structures in-field rather than making indirect conclusions.

The room temperature in-plane (IP) and out-of-plane (OOP) hysteresis loops of Nd–Dy–Fe–Co–B single layer, well-coupled and decoupled samples are shown in Figs. 17(a)–17(c).[48] Although a smooth hysteresis loop is presented in the OOP direction (Fig. 7(b)), a kink has appeared at the IP direction, which indicates that the interactions between SM and HM are changed with the measuring directions. Strong coupling leads to good squareness and higher remanence. In the demagnetiazation process, the interaction energy along the OOP direction, which can be estimated by the energy of magnetization reversal from remanence to the nucleation field, is given as

$$\sigma_i = \int_{M_N}^{M_r} H_{ex}\,\mathrm{d}M,$$

where M_r is the remanence, M_N is the magnetization at nucleation field, and H_{ex} is the external field.[22,49] When SM and HM layers are well coupled, σ_i is about 3–11 mJ/m^2, which is four times larger than that of the decoupled sample.

The families of FORCs in the out-of-plane direction of the films are shown in Figs. 17(d)–17(f). The acquisition of a FORC begins by saturating the system in a positive applied field. Then the applied field is decreased to a reversal field H_r, and the magnetization M is measured starting from H_r back to positive saturation. In Fig. 17(d), the Nd–Dy–Fe–Co–B single layer shows irreversible switching at a reversal field $H_r = -1.5$ T, where the FORCs deviate from the major loop after positive saturation of the samples.[50] Hereafter, nucleation of the domain starts, which indicates that the applied field does not bring the system back into the original state when the applied field returns back. For the well-coupled film (20 nm MgO spacer), the same process of irreversible switching starts to occur at a reversal field $H_r = -0.7$ T. In Fig. 17(f), the decoupled film (70 nm MgO spacer) shows two separate irreversible switchings at $H_r = 0.4$ T and -0.6 T, respectively. The positive value of H_r is attributed to the SM phase, which indicates initial nucleation before 0.4 T of applied field independently, as a result, the exchange-spring behavior between SM and HM magnets does not occur.

The as-prepared state is almost a virgin state (thermal demagnetized). The MFM images of the Nd–Dy–Fe–Co–B single layer and the well-coupled and decoupled multilayer films are shown in Figs. 17(g)–17(i), respectively. The scanned area is 10 μm×10 μm. The yellow and brown contrast corresponds to out-of-plane up and down magnetizations, respectively. The image of the Nd–Dy–Fe–Co–B single layer (Fig. 17(g)) is characterized by a stripe domain with a magnetization oriented preferentially out-of-plane. The average domain width is 90 nm, which is a little larger than the grain size (60 nm). This phenomenon indicates the existence of interaction domains, but the magnetic coupling between grains is weak.[51,52] The size of the stripe domains extends when a 10 nm SM Fe layer and a 20 nm MgO spacer layer are added (well-coupled sample, Fig. 17(h)). This indicates that the easy direction of magnetization may slightly tilt away, but is still mainly out-of-plane. When the spacer layer increases to 70 nm, the MFM image of the decoupled film (Fig. 17(i)) presents a quite different domain pattern from those shown in Figs. 17(g) and 17(h). A micron-size domain with clear light and dark contrast is observed in the pattern. In addition to the micron-size domain, small labyrinth stripe domains are also distributed in the pattern. This phenomenon of the two different domains coexisted in one pattern can be considered as characteristic of decoupled phases.[53]

In order to understand the behavior of domains under a specific field, the applied magnetic field was applied perpendicular to the film during the measurement of the MFM images. In Figs. 18, the domain patterns of the well-coupled sample were obtained in the same surface region, as shown

in Fig. 18(a). In Figs. 18(b)–18(i), the applied field is continuously decreased from the positive saturation, where the yellow and blue colors correspond to out-of-plane up and down magnetizations, respectively. When the applied field is between 1 T and 0.1 T, as shown in Figs. 18(b) and 18(c), a nanosize stripe structure of the domains is observed. Upon decreasing field, the domains parallel to the field weaken and reverse to the opposite direction as marked by the red ellipses in Figs. 18(c) and 18(d). When the applied field decreases to −0.5 T, near the irreversible switching field, new domains begin to nucleate, as marked by the red ellipses in Fig. 18(e). The new domains propagate and the residual domains are being annihilated. It can be seen from Fig. 18(f) that the domains have become larger at −1 T. When the applied field reaches −1.5 T, the magnetization follows the major loop, and the domains begin to annihilate gradually (see the red ellipses in Figs. 18(f) and 18(g)). Finally, at −2.5 T, the blue color covers most of the image (Fig. 18(i)), which indicates that the magnetization of the domains is nearly fully aligned.

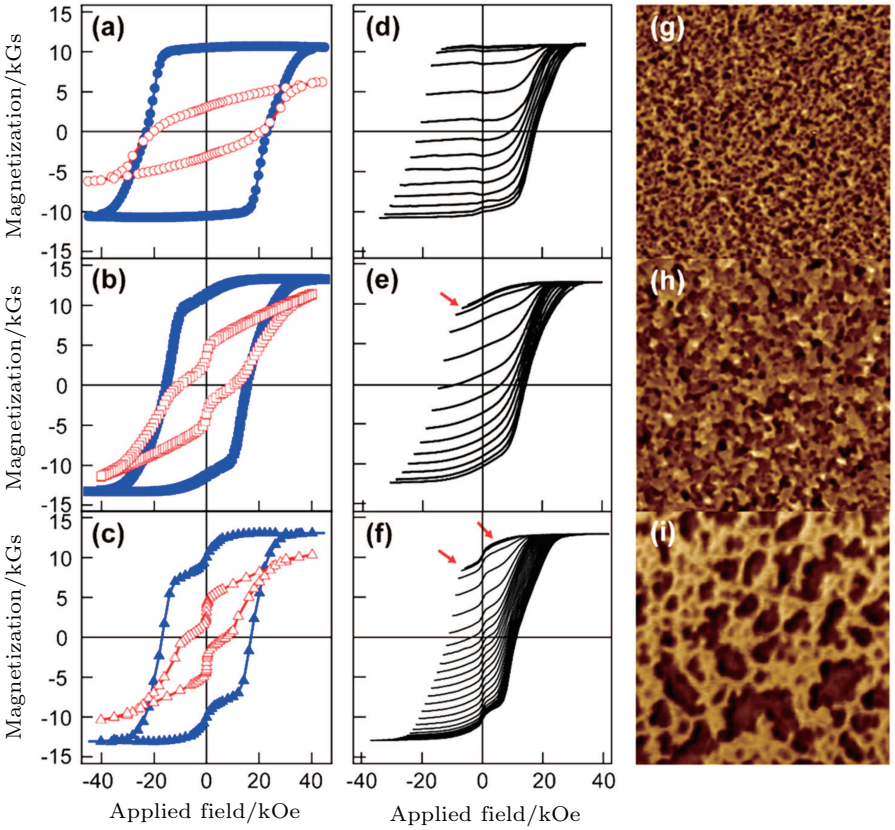


Fig. 17. (color online) The room temperature IP and OOP hysteresis loops (a)–(c), families of FORCs (d)–(f), and MFM images in the as-prepared state (g)–(i). For the Nd–Dy–Fe–Co–B single layer (a), (d), and (g), the well-coupled sample (b), (e), and (h), and the decoupled sample (c), (f), and (i), respectively.[48]

Compared with the results on the well-coupled sample, the behavior of the decoupled sample can be divided into two separated nucleation processes. The first nucleation process begins before the applied field is decreased to 1.2 T. In Figs. 19(b) and 19(c), the micron-size domains are marked with yellow and blue colors, while weak signs of nanosize domains are distributed between these patterns. The propagation process of the micron-size domains is marked in the red ellipses at 1.2 T and 1.1 T. When the field decreases to −0.1 T (Fig. 19(d)), the domains begin to switch and annihilate. Nucleation of new domains occurs at −0.7 T (Fig. 19(e)). The new domains continuously propagate (see Figs. 19(f) and 19(g)) until the applied field is near the coercivity (see Figs. 19(h) and 19(i)), where the annihilation process starts to occur.

In a simplistic consideration, the domain pattern reflects the competition of dipolar magnetostatic energy, Zeeman energy, and domain wall energy. Based on the micromagnetic theory,[54,55] the ferromagnetic multilayers with perpendicular magnetic anisotropy (PMA) always present stripe domains. By assuming the stripe period $D = d_{\rm up} + d_{\rm down}$ and dimensionless parameter $q = (d_{\rm up} - d_{\rm down})/D$, where $d_{\rm up}$ and $d_{\rm down}$ are up and down domain widths, the energy density of a stripe domain can be written in the following form:[56,57]

$$w_{\rm s} = 8\pi M^2 \frac{l_{\rm c}}{D} - HMq + 2\pi M^2 \tilde{N}(D,q).$$

Here $l_{\rm c} = \sigma/4\pi M^2$ is the characteristic length, defined by the ratio of wall-energy density σ and the magnetostatic energy density $2\pi M^2$. The first term describes the domain wall energy density of the stripe domain pattern. The second term is the Zeeman term. It indicates that by increasing the external

magnetic field, the domains which are aligned parallel to the field grow while the oppositely aligned domains get smaller. The last term is associated with the dipolar magnetostatic interactions between pairs of the "charged" planes bounding the layers. $\tilde{N}(D,q)$ is an effective demagnetizing factor. Generally, the domain wall energy density increases with decreasing domain size, thus a strong dipolar interaction favors smaller domains.

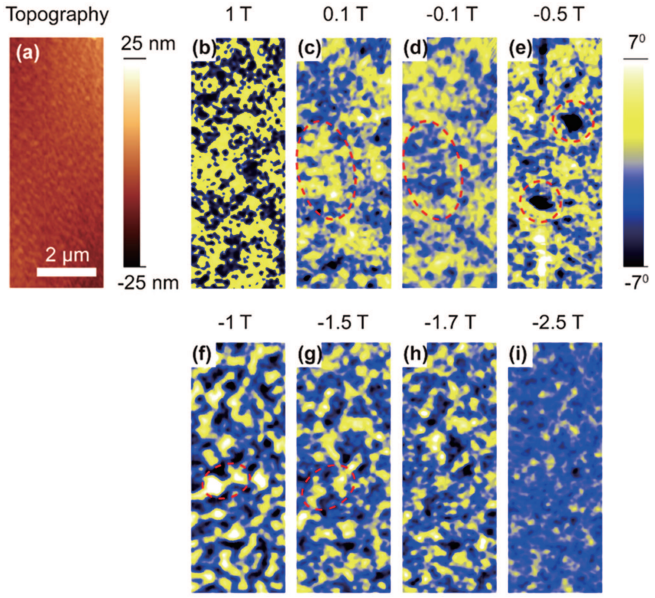


Fig. 18. (color online) MFM images of the well-coupled sample. The AFM topography (a) and the MFM images scanned at 1 T (b), 0.1 T (c), −0.1 T (d), −0.5 T (e), −1 T (f), −1.5 T (g), −1.7 T (h), and −3 T (i). All MFM images are taken from the same area.[48]

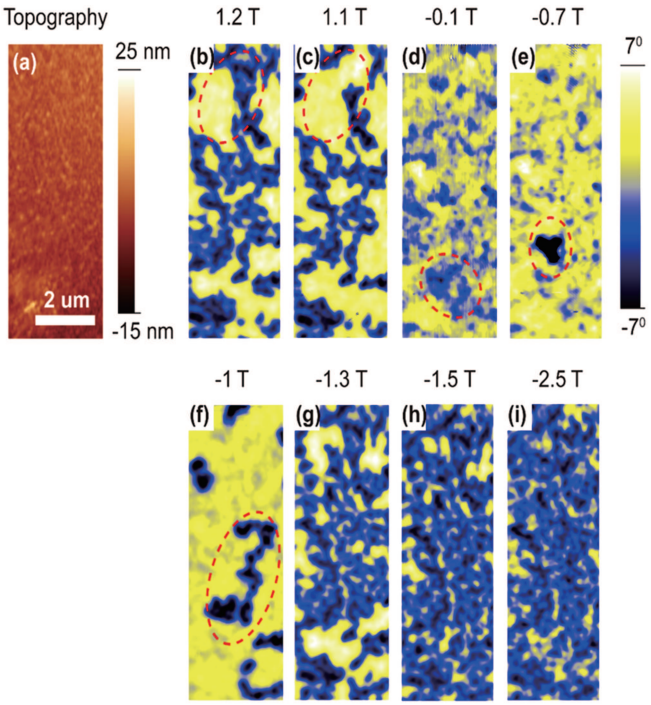


Fig. 19. (color online) MFM images of the decoupled sample. The AFM topography (a) and the MFM images scanned at 1.2 T (b), 1.1 T (c), −0.1 T (d), −0.7 T (e), −1 T (f), −1.3 T (g), −1.5 T (h), and −2.5 T (i). All MFM images are taken from the same area.[48]

It should be noted that without the HM layer, the magnetization of SM thin film is aligned in-plane and there should be no stray field detected by MFM technology. But in both the well-coupled and decoupled nanocomposite multilayers, the out-of-plane magnetization is shown at the surface of the SM layer. It is concluded that although the domains of SM layer are not aligned parallel with the coherent HM layers in decoupled multilayer, a small angle between the moments of SM and HM layers is performed due to the existence of the weak dipolar interactions between SM and HM layers. Therefore, the magnetization of the SM layer contributes to the domains along out of plane.

To investigate the magnetization reversal behavior between adjacent layers, the patterned micron-size disk arrays were prepared. The lithography-patterned arrays of soft Fe disks onto continuous Nd–Dy–Fe–Co–B hard-magnetic layer are shown in Fig. 20(a) and 20(b). The diameters of the disks are 3 μm and the distance between the central of the adjacent two disks is larger than 4 μm, which makes sure there is no interactions between disks. Results on the well-coupled and decoupled SM disks are shown in Figs. 20(c) and 20(d) under different applied fields. At 1.2 T, in both Figs. 20(c) and 20(d), the MFM image exhibits a different contrast between the surface of the Fe disk and the surrounding Nd–Dy–Fe–Co–B film. Here, the yellow and blue colors represent a relative phase intensity between SM disk and HM layer. Thus, the line profiles (Figs. 20(e) and 20(f)) extracted from this applied field show opposite phase degrees along the Fe disk surface with the lower Nd–Dy–Fe–Co–B layer. As the MFM tip can only detect external stray fields, the large contrast of the phase signal may be associated with the different magnetization of the Fe-disk surface and the Nd–Dy–Fe–Co–B film.[58] Upon decreasing the applied field, in the well-coupled disk, the rim of the Fe disk becomes blurry at the remanent magnetization state and the ferromagnetic labyrinth stripe domains at the edge of the disk are aligned continuously. This indicates that the magnetization of the SM disk and the adjacent HM layer are parallel, which is favored by strong dipolar fields. In addition, the signal intensities of SM and HM layers converge into the same level, as shown in Fig. 20(e). For the decoupled disk, a clear rim with incoherent orientation of the magnetization between the Fe disk and Nd–Dy–Fe–Co–B single layer is observed. Unlike the PMA antiferromagnetic multilayer, in which magnetization of adjacent layers is antiparallel,[54] the magnetization orientation of micron-size domain in decoupled disk is random. Upon increasing the field along the negative direction, the different nucleation behaviors of the well-coupled and decoupled disks are observed. In Fig. 20(c), the nucleation process happens on the Fe disk and Nd–Dy–Fe–Co–B layer nearly at the same time at −0.8 T. Next, the propagation and annihilation processes are presented at −1.1 T and −1.8 T, respectively. Finally, a clear negative phase signal ap-

pears again on the Fe disk. However, in the decoupled disk, the domains of the Fe disk propagate and the magnetization is nearly fully aligned at −0.5 T, while nucleation initially starts in the Nd–Dy–Fe–Co–B layer. We also measured another disk and the same result was achieved. In addition, it is found that the phase signal intensity of the Nd–Dy–Fe–Co–B layer is much larger than that in the Fe disk, as shown in Fig. 20(f).

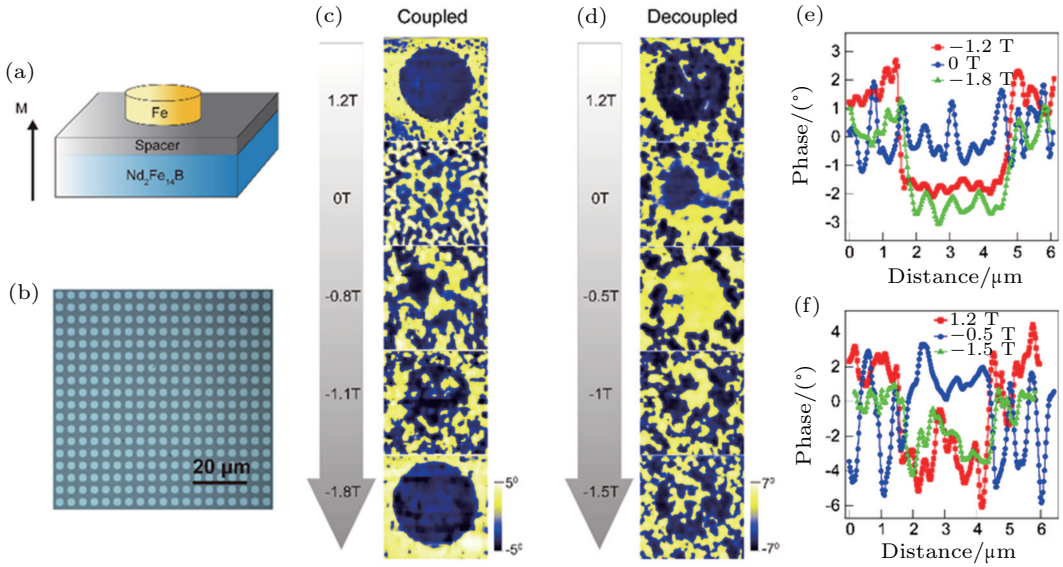


Fig. 20. (color online) The MFM images of the micron-size SM disk. (a) Schematic illustration of lithography-patterned arrays of soft Fe disks onto continuous Nd–Dy–Fe–Co–B hard-magnetic layer, and the well-coupled and decoupled structures are tuned by inserting a critical thickness of spacer layer. (b) Optical image of the disks array prepared by lithography technology. (c) and (d) The in-field MFM images of the well-coupled and decoupled disks, respectively. (e) and (f) Line profiles extracted from MFM images shown in panels (c) and (d), respectively.[48]

It is concluded that a strong dipolar interaction between SM and HM layers favors smaller domains. Micron-sized nanocomposite structures consisting of the soft Fe disks and the continuous Nd–Dy–Fe–Co–B film are manipulated by lithography. The Fe disks coupled with the Nd–Dy–Fe–Co–B exhibit a coherent magnetization reversal. While the decoupled disk magnetization of SM/HM layers is independent and nucleation initially starts from the Nd–Dy–Fe–Co–B layer at negative descending field. Furthermore, it is found that a strong anisotropy of the Nd–Dy–Fe–Co–B layer decreases the interaction length. These results provide a microscopic understanding of magnetization reversal in the long-ranged dipolar interactions between soft- and hard-magnetic phases.

In summary, the coherent switching process of the hard- and soft-magnetic phases has been presented by altering the thickness of different kinds of spacer layers. However, an antiferromagnetic spacer layer may weaken the interaction between the ferromagnetic layers and the effective interaction length is decreased. In addition, the ratios of the irreversible component dependent on the thickness of the spacer layer illustrate that the shape anisotropy is important in the long-range interactions in a soft- and hard-magnetic layer system. The present observations may contribute to a new discussion on understanding the mechanism of long-range soft- and hard-magnetic interactions in anisotropic nanocomposite magnets.

3. Anisotropic $SmCo_5$ based nanocomposite permanent multilayer magnets

The $SmCo_5$ compound possesses huge uniaxial magnetocrystalline anisotropy ($K_u \approx 17.2$ MJ/m^3) and anisotropy field ($\mu_0 H_A \approx 35$ T), so it can generate large coercivity if crystal grains are magnetically isolated in thin films.[59,60] Depending on compositions and preparation conditions, various Sm–Co phases, such as $SmCo_3$, Sm_2Co_7, $SmCo_5$, $SmCo_7$, and Sm_2Co_{17}, which show different anisotropy fields, can be formed. Among them, the $SmCo_5$ phase has the highest anisotropy field. A high coercivity has been achieved by depositing Sm–Co onto a heated substrate[61] or by annealing the film deposited at room temperature.[62–64] In addition, the easy axis (c-axis) of $SmCo_5$-based thin films can be manipulated by using different substrates. The c-axis in-plane (IP) geometry was reported in the films epitaxially grown on MgO (110) single crystal substrates with W[65] and Cr[66] buffer layers. The c-axis out-of plane (OOP) geometry was realized by growing $SmCo_5$ films on Al_2O_3(001) single-crystal substrates with Ru buffer layers.[67] Since $SmCo_5$ as a hard phase couples with hard phases such as Fe, Co, and FeCo in the multilayer films, the related work has been performed.[68–73] Although the exchange coupling and machanism of coercivity have been investigated in these early reports, the maximum energy product of the exchange coupled films is not high. In this part, we will review recent work on anisotropic $SmCo_5$ based nanocompos-

ite permanent multilayer magnets in which the energy product of the films has been improved obviously.

Zhang *et al.*[74] selected $SmCo_5$ as a hard phase and Fe as a soft phase. The multilayer films were prepared by sequentially depositing Sm–Co, Cu, and Fe layers on a 100-nm-thick Cr underlayer on a thermally oxidized Si wafer. The structure of the Sm–Co layer was amorphous in the as-deposited condition, so the as-deposited films were Cr (50 nm)/[a-(Sm–Co) (9 nm)/Cu (x nm)/Fe (5 nm)/Cu (x nm)]$_6$/Cr (100 nm)/a-SiO_2, where "a" indicates amorphous phase. Then, the films were heat treated at temperatures ranging from 450 °C to 525 °C for 30 min. Figure 21 shows the in-plane and out-of plane hysteresis loops of the film with $x = 0.5$ that was annealed at 450 °C for 30 min. The film exhibits a strong in-plane anisotropy that is consistent with the XRD results. The in-plane hysteresis loop shows good squareness in the second quadrant, implying that this kind of film has the potential to be used as a permanent magnet. H_c of 7.24 kOe and $(BH)_{max}$ of 32 MGOe were obtained in this film, which is larger than the theoretical limit for a $SmCo_5$ single phase magnet, 28.8 MGOe. This value is also larger than that of the commercial $SmCo_5$ and $Sm(Co,Fe,Cu,Zr)_7$ type sintered magnets. By replacing Fe with $Fe_{65}Co_{35}$ or adjusting the thickness of the hard and soft layers, it will be possible to enhance the $(BH)_{max}$ further. This work has demonstrated that there is a potential to develop high performance exchange spring magnets by optimizing nanocomposite microstructures.

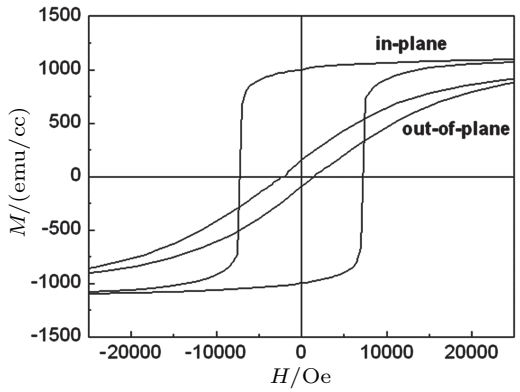


Fig. 21. (color online) In-plane and out-of-plane hysteresis loops of the film with $x = 0.5$ annealed at 450 °C for 30 min.[74]

As a very promising approach, fully epitaxial trilayers based on the hard magnetic $SmCo_5$ phase and soft magnetic Fe have been realized,[75] which possess a unique alignment of the $SmCo_5$'s easy axis throughout the whole layer stack and reach energy densities of 224 kJ/m^3 (28 MGOe). In order to enhance the energy density $(BH)_{max}$ as a key property for permanent magnet applications, exchanged-coupled trilayers of $SmCo_5$/Fe/$SmCo_5$ with fixed $SmCo_5$ layer thickness (25 nm) and varying soft magnetic Fe film thickness have been epitaxially grown by pulsed laser deposition on Cr buffered MgO (110) substrates.[76] A real view of the layer architecture is displayed in the TEM bright field cross sectional image of the sample with 12 nm nominal Fe (Fig. 22). The individual Cr, $SmCo_5$, and Fe layers on top of the MgO substrate are clearly visible. The interfaces of the $SmCo_5$ layers toward the outer Cr buffer or cover layer are well defined and smooth, which leads to a well determined total magnetic layer thickness of 60.4 ± 0.9 nm for this sample. Interestingly, the interface between the intermediate FeCo layer and the neighboring $SmCo_5$ layers typically is rough along the length of the film, leading to a local thickness variation of the intermediate FeCo layer (see dashed lines as a guide for the eye). The interface was identified from high resolution images revealing lattice fringes and the crystal structure of either bcc or hcp type. Within the intermediate bcc layer, one cannot distinguish between pure Fe or the FeCo solid solution, but the latter is expected from the RBS results.

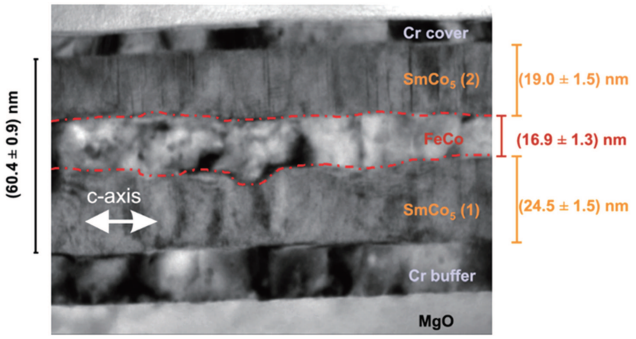


Fig. 22. (color online) Transmission electron microscopy cross sectional image of a trilayer with nominal 12 nm Fe along the magnetic easy axis (c-axis).[76]

A selection of magnetic hysteresis curves measured along the MgO[001] direction is given in Fig. 23.[76] For a pure 50 nm single $SmCo_5$ layer, the hysteresis possesses a square shape with a coercive field of 2.76 T. The remanent polarization of 0.98 T is very close to the known saturation magnetization ($J_s = 1.05$ T) of $SmCo_5$ bulk material. With increasing Fe thickness, a significant increase of remanence and a strong decrease in coercivity are observed. Whereas for $d_{Fe} = 6.3$ nm, the soft layer is perfectly coupled to the hard magnetic layer with a rectangular hysteresis loop; for $d_{Fe} = 12.6$ nm, a drop in the curve indicates rotational processes in the soft magnetic phase. As the two $SmCo_5$ layers can just couple a certain amount of Fe, a spin spiral is formed in the soft phase, which is visible in a nucleation field H_n at which the magnetization in the center of the Fe layer begins to rotate toward the external field. H_n gets smaller with increasing Fe thickness. Although this rotation is reversible,[75] it leads to a large reduction in energy density. The small step at zero field for $d_{Fe} = 6.3$ nm is due to the sample mounting.

The coercive field and the nucleation field as a function of the Fe thickness measured along the easy axis (for all samples)

are shown in Fig. 24.[76] The observed strong decline is in accordance with the theoretical prediction of Leineweber and Kronmüller[77] and other numerical simulations.[78–80] However, in the calculations of Leineweber and Kronmüller,[77] as the soft layer thickness below the Bloch wall width of the hard magnetic phase ($\delta_w^h = 3.4$ nm) should leave the nucleation field unaltered. This is in contrast to the observation in this work, where already for an Fe thickness of $d_{Fe} = 3$ nm H_n is reduced over that of the single $SmCo_5$ layer. With a further increase in d_{Fe} of 3 nm, an additional reduction in H_c of 30% can be observed. Above a critical Fe thickness of 8.8 nm (dashed line), the coercive field and the nucleation field take different values, which indicates the change in magnetic coupling from the single phase behavior to an exchange spring regime. This is analog to micromagnetic calculations,[79] which show that a hard/soft magnetic layer system has only one common irreversible switching field for thin soft layers (rigid-magnet (RM) regime) and then enters the exchange-spring regime for thicker soft layers with clearly distinguishable nucleation and irreversibility fields. It should be noted that the coercive field in these samples such as in all multidomain samples is reduced with respect to a theoretical switching field. As a consequence, the coercive field of a trilayer might be lower than the theoretical nucleation field and may mask its existence. Such a scenario has been identified for a trilayer with 6 nm Fe in comparison with micromagnetic calculations.[80] Thus, the experimentally observed single phase regime is extended to a larger soft layer thickness compared to the theoretical RM regime. It should be noted that for this sample, the active layer thickness is reliably given by TEM to 60.4 ± 0.9 nm (see Fig. 22), which corresponds to a maximum energy density of 346 ± 10 kJ/m^3. Including the 3% spread due to the above mentioned sample area and VSM signal precision errors, the total error in $(BH)_{max}$ is about 9% and leads to 346 ± 31 kJ/m^3. Therefore, the largest maximum energy density of 312 ± 50 kJ/m^3 claimed in this work is rather underestimated.

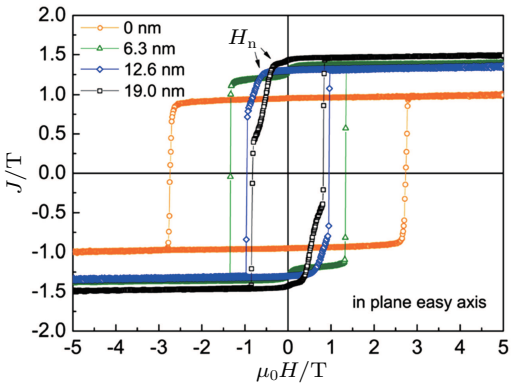


Fig. 23. (color online) Polarization J as a function of the external field $\mu_0 H$ measured along the MgO[001] orientation (in plane easy axis) for $SmCo_5$ (25 nm)/Fe (x nm)/$SmCo_5$ (25 nm) trilayers with $x = 0$, 6.3, 12.6, and 19.0.[76]

In order to investigate the effects of easy axis orientations on the coercivities and their thermal stabilities, Cui *et al.*[81] prepared different morphologies and c-axis geometries of $Sm(Co_{0.9}Cu_{0.1})_5$ (50 nm) single-layer (SL) films and $Sm(Co_{0.9}Cu_{0.1})_5/Fe_2Co$ exchange coupled bi-layer films by co-sputtering Sm(99.5%), Co(99.9%), and Cu(99.9%) targets onto Cr (20 nm)-buffered MgO (110) (or Ru (20 nm)-buffered Al_2O_3(012)) single-crystal substrates respectively. Figure 25 shows hysteresis loops of MgO/Cr (20 nm)/Sm$(Co_{0.9}Cu_{0.1})_5$ (50 nm)/Fe_2Co (x nm)/Cr (20 nm) films with c-axis in-plane (IP) geometry ($x = 3$ (a), 5 (b), 8 (c), and 10 (d)) and Al_2O_3/Ru (20 nm)/Sm$(Co_{0.9}Cu_{0.1})_5$ (50 nm)/Fe_2Co (x nm)/Ru (20 nm) films with c-axis out-of-plane (OOP) geometry ($x = 3$ (e), 5 (f), 8 (g), and 10 (h)). The IP and OOP hysteresis loops indicate the c-axis geometries consistent with those observed from XRD results. In the MgO/Cr (20 nm)/Sm$(Co_{0.9}Cu_{0.1})_5$ (50 nm)/Fe_2Co (10 nm)/Cr (20 nm) film, the demagnetization process is continuous along both IP and OOP directions as shown in Fig. 25(d). In the Al_2O_3/Ru (20 nm)/Sm$(Co_{0.9}Cu_{0.1})_5$ (50 nm)/Fe_2Co (10 nm)/Ru (20 nm) film (see Fig. 25(h)), the demagnetization process is continuous along the OOP direction. Along the in-plane direction, a two-step behavior is observed on the hysteresis loop near zero field.

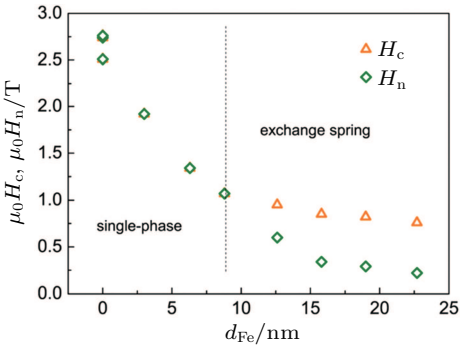


Fig. 24. (color online) Coercive field H_c and nucleation field H_n as a function of the Fe thickness d_{Fe}. The dashed line represents the critical point where the change of the single phase to the exchange spring behavior occurs.[76]

To understand the physical mechanism, schematics of different c-axis geometries in exchange coupled bilayer films are plotted in Figs. 26(a) and 26(b). Exchange coupling energy E_{ex} and magnetostatic coupling energy E_{static} are dependent on the angle between hard magnetic moment and soft-magnetic moment, which are expressed as

$$E_{ex} = -A_{ex} \boldsymbol{m}_k \cdot \boldsymbol{m}_{i,j},$$

$$E_{static} = \sum_{i=0}^{i=n} \sum_{j=-k}^{j=k} \frac{\mu_0}{4\pi r^3} \times \left[\boldsymbol{m}_k \boldsymbol{m}_{i,j} - \frac{3}{r^2} (\boldsymbol{m}_k \cdot \boldsymbol{r})(\boldsymbol{m}_{i,j} \cdot \boldsymbol{r}) \right].$$

Exchange coupling is a short-range interaction because exchange stiffness A_{ex} decays exponentially within several nanometers.[31,82,83] On the other hand, magnetostatic coupling is a long-range interaction due to the integration of every

moment in both hard/soft-magnetic layers as seen from Fig. 26 and E_{static} expression. Its long-range feature was experimentally confirmed in the Ta spacer of $Nd_2Fe_{14}B$/a-Fe multilayer films.[31,84] For simplicity, the total coupling energies in different c-axis geometries between neighboring hard-magnetic moment $\boldsymbol{m}_h$ and soft-magnetic moment $\boldsymbol{m}_{0,0}$ are compared in Fig. 26(c). Obviously, in both geometries, E_{ex} is negative and causes the parallel alignment of hard/soft magnetic moments. On the other hand, in c-axis OOP geometry, E_{static} is negative compared with the positive one in the c-axis IP geometry, leading to energetically preferred and stronger coupling in the c-axis OOP geometry. Therefore, higher coercivities are achieved in the bilayer films with c-axis OOP in the $Sm(Co_{0.9}Cu_{0.1})_5$ layer than that with the c-axis IP geometry. In the OOP exchange coupling geometry, the observed two-step behavior in Fig. 25(h) can also be explained by the magnetostatic coupling. Along the in-plane direction of OOP exchange coupling geometry, forced by the external field, the moments in hard-magnetic phase are tilted away from easy axis and close to in-plane direction. When the external field is swept to zero fields, confined by the out-of-plane easy axis, the moments in hard-magnetic phase tend to be back to easy axis. Meanwhile, the soft-magnetic moments also tend to be reversed due to the repulsive interaction caused by the magnetostatic coupling when the hysteresis loops are measured along the in-plane direction. Therefore, a non-uniform magnetization reversal process happens, leading to the two-step behavior observed in IP hysteresis loops as shown in Fig. 25(h).

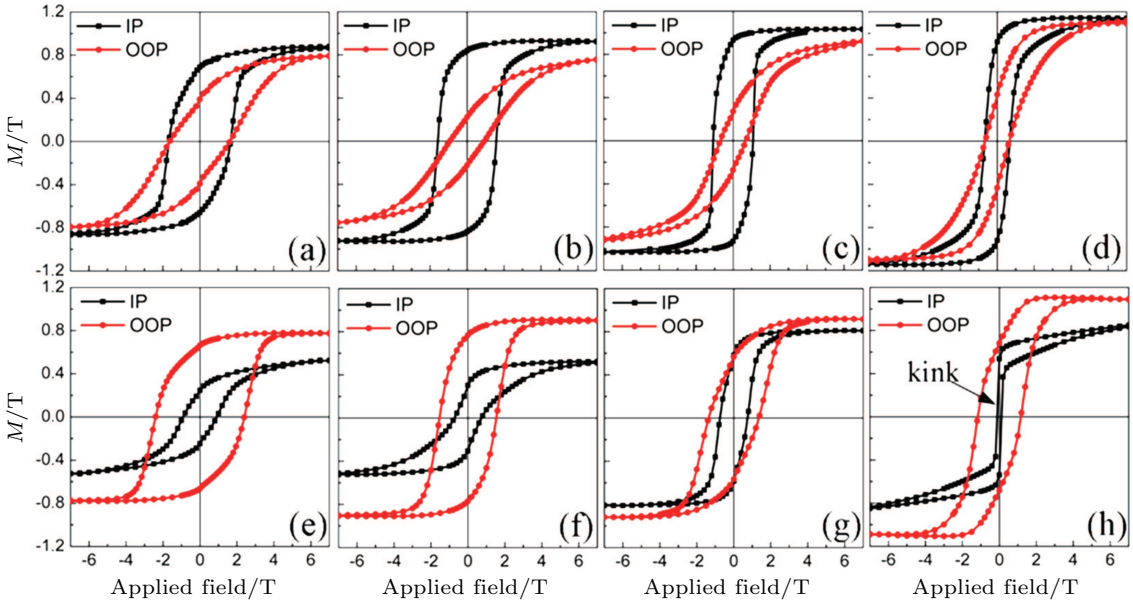
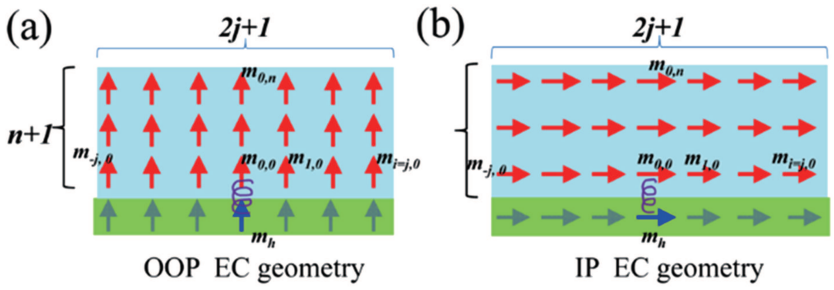


Fig. 25. (color online) Hysteresis loops of MgO/Cr (20 nm)/$Sm(Co_{0.9}Cu_{0.1})_5$ (50 nm)/Fe_2Co (x nm)/Cr (20 nm) films with c-axis in-plane (IP) geometry ($x = 3$ (a), 5 (b), 8 (c), and 10 (d)) and Al_2O_3/Ru (20 nm)/$Sm(Co_{0.9}Cu_{0.1})_5$ (50 nm)/Fe_2Co (x nm)/Ru (20 nm) films with c-axis out-of-plane (OOP) geometry ($x = 3$ (e), 5 (f), 8 (g), and 10 (h)).[81]



(c)

	E_{ex}	E_{static}
IP EC	$-A_{ex}m_hm_{0,0}$	$\frac{\mu_0}{4\pi}\frac{m_hm_{0,0}}{r^3}$
OOP EC	$-A_{ex}m_hm_{0,0}$	$\frac{\mu_0}{4\pi}\frac{-2m_hm_{0,0}}{r^3}$

Fig. 26. (color online) Schematics of c-axis out-of-plane (OOP) (a) and in-plane (IP) (b) exchange coupling (EC) geometries in exchange-coupled bilayer films. (c) Comparisons of exchange coupling energy (E_{ex}) and magnetostatic energy (E_{static}) between moment $\boldsymbol{m}_h$ in hard-magnetic layer and $\boldsymbol{m}_{0,0}$ in soft-magnetic layer as shown in Figs. 26(a) and 26(b).[81]

In summary, the effective critical correlation length (L_{ex}^{eff})[16] and effective interaction length (L^{eff})[31] are very short due to the huge uniaxial magnetocrystalline anisotropy of the $SmCo_5$ phase. So the direct exchange coupling between hard and soft layers is dominant in nanocomposite hard/soft multilayer films. Thus, it is very hard to insert a space layer between $SmCo_5$ and soft layers for ensuring the effective exchange coupling between anisotropic hard phase and soft phase, in other words, we will not add enough thick soft layer into this system. Although largely enhanced energy density has been obtained in epitaxial $SmCo_5$/Fe/$SmCo_5$ exchange spring trilayers, basically, the easy *c*-axis of $SmCo_5$ lies in plane of the films due to the $SmCo_5$ crystal structure. Because a soft layer is easy to diffuse into the $SmCo_5$ layer during the deposition or subsequent annealing, it can be challenging in realizing anisotropic $SmCo_5$/(Fe or FeCo) multilayers with higher energy product in the future.

4. Anisotropic rare-earth free based nanocomposite permanent multilayer magnets

Rare-earth free based permanent magnets such as AlNiCo, ferrite, FePt, MnAlC, and MnBi have been investigated. As a hard phase of anisotropic rare-earth free based nanocomposite permanent multilayer magnets, it is of strong uniaxial anisotropy and can be grown on the substrate along the easy axial direction. So we will only review the anisotropic FePt and MnBi based nanocomposite permanent multilayer magnets in this part.

It is known from the equilibrium phase diagram of the Fe–Pt binary alloy system that for the ordered alloy FePt, it crystallizes in the fct $L1_0$ structure with the high magnetocrystalline anisotropy constant K_1 (> 1 MJ/m^3), but it does not coexist with α-Fe. Liu *et al.*[85] sputtered Fe layers having twice the thickness of the Pt layers to prepare multilayers with an atomic Fe-to-Pt ratio of about 2:1. To avoid excessive grain growth, a special rapid thermal annealing process that includes more than one step of treatment was adopted. An extremely large energy product corrected by an effective demagnetizing factor in the perpendicular direction was achieved at room temperature, in which the soft phase is Fe_3Pt and it belongs to isotropic. Jiang *et al.*[86] reported that interlayer exchange coupling between FePt and Fe layers through a Ru spacer was obtained with an oscillation period of about 1 nm. Magnetic properties of FePt thin films with different nominal thicknesses deposited on MgO (1 1 0) substrates at 400 °C showed that 12.5 nm thick FePt film had both high coercivity and good squareness. In FePt/Ru/Fe trilayers, ferromagnetic coupling between the two magnetic layers was achieved with a 0.5 nm thick Ru layer, and the saturated magnetization was largely improved after using interlayer exchange coupling with Fe while the coercivity changed little, which indicated that indirect exchange spring was a promising approach for high-performance magnets. However, the exchange coupling strength trailed off with Fe content increasing, and a hysteresis loop with good rectangular in FePt/Ru/Fe trilayers can be obtained when the thickness ratio of FePt/Fe is larger than 6. The hysteresis loops with good rectangular have also been obtained in $(FePt/Ru/Fe)_{10}$ multilayers even when the thickness ratio of FePt/Fe is 1. Liu *et al.*[87] reported that two-phase nanostructures of hard $L1_0$-ordered FePt and soft iron-rich fcc Fe–Pt are investigated experimentally and by model calculations. The Fe–Pt thin films were produced by epitaxial co-sputtering onto MgO and have a thickness of about 10 nm. They form two-phase dots that cover a large fraction of the surface but are separated from each other. X-ray diffraction and TEM show that the *c*-axis of the phase FePt is aligned in the direction normal to the film plane. The experimental and theoretical hysteresis loops indicate archetypical exchange coupling, and excellent magnetic properties are obtained. The largest values of coercivity, saturation magnetization, and nominal energy product obtained in the samples studied are 51 kOe, 1287 emu/cc, and 54 MGOe, respectively.

In order to realize anisotropic FePt based nanocomposite permanent multilayer magnets, L1(0)-FePt film with 20 nm was deposited on (001) orientated single crystal MgO substrate with *in-situ* heating at 830 °C, and then spacer layer Ag and different thickness soft layer with Fe was deposited at room temperature. Figure 27 shows magnetic hysteresis loops at room temperature for the out of plane MgO (substrate)/FePt (20 nm)/Ag (x nm)/Fe (2 nm)/Ag (2 nm) films. It is clear that the obvious decoupling behavior occurs at the film with $x = 0$. For $x = 1$, a good squareness of hysteresis loop is found due to interlayer coupling between hard and soft phase layers. Its coercivity is the same as that of the single FePt film. For $x = 2$, a poor squareness of hysteresis loop is observed, so the thickness of the spacer layer is 1 nm in favor of effective coupling between FePt and Fe layers. Figure 28 shows the x-ray diffraction patterns for the MgO (substrate)\FePt (10 nm)\MgO (2 nm)\Fe (2 nm)\ MgO (2 nm)\FePt (10 nm)\MgO (5 nm) film deposited at 750 °C. Three strong peaks are observed: FePt (001), FePt (002), and MgO (002). It is clear that ordered $L1_0$ FePt phase is out of plane alignment in the nanocomposite film. Magnetic hysteresis loops at room temperature for the out of plane MgO (substrate)\FePt (10 nm)\MgO (2 nm)\Fe (2 nm)\ MgO (2 nm)\FePt (10 nm)\MgO (5 nm) film deposited at 750 °C is given in Fig. 29. It is found that the spacer layer MgO with 2 nm prevents diffusion between Fe and PtFe layers and insures the form and alignment of the $L1_0$ FePt phase. Clear coupling between Fe and PtFe layers is observed. It is concluded that this interaction is indirect.

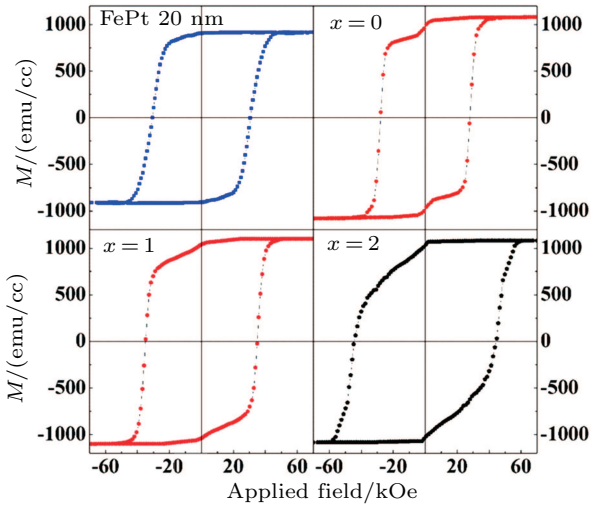


Fig. 27. (color online) Magnetic hysteresis loops at room temperature for the out of plane MgO (substrate)/FePt (20 nm)/Ag (x nm)/Fe (2 nm)/Ag (2nm) films.

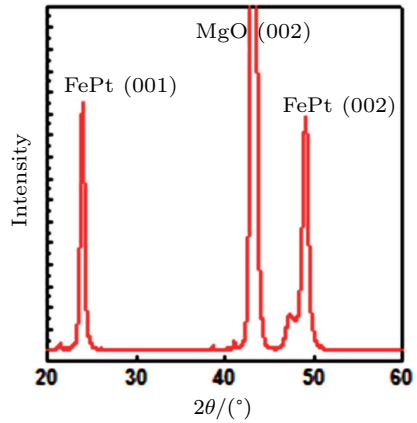


Fig. 28. (color online) X-ray diffraction patterns of MgO (substrate)\FePt (10 nm)\MgO (2 nm)\Fe (2 nm)\MgO (2 nm)\FePt (10 nm)\MgO (5 nm) film deposited at 750 °C.

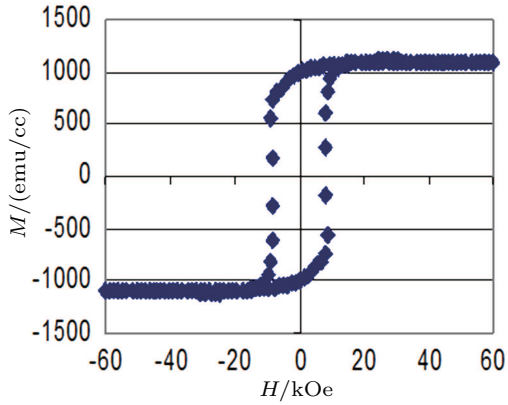


Fig. 29. (color online) Magnetic hysteresis loops at room temperature of the out of plane MgO (substrate)\FePt (10 nm)\MgO (2 nm)\Fe (2 nm)\MgO (2 nm)\FePt (10 nm)\MgO (5 nm) film deposited at 750 °C.

The low temperature phase (LTP) of MnBi is a ferromagnetic intermetallic compound which crystallizes in the NiAs-type hexagonal crystal structure.[88–90] LTP MnBi has attracted a great deal of attention due to the unusual magnetic properties, for example, a magnetocrystalline anisotropy (H_A) of 9.0 T and a coercivity (H_C) of 1.8 T have been achieved for melt-spun ribbons at 550 K,[91] which are much larger than those of the Nd–Fe–B magnet under the same conditions. Hence, LTP MnBi has an exciting prospect as a non-rare-earth permanent magnet material for high temperature applications,[92] and experimental investigations on the effect of Fe impurity on the structural, magnetic and electron transport properties of MnBi films. Kharel *et al.* reported experimental investigations on the effect of Fe impurity on the structural, magnetic, and electron transport properties of MnBi films.[93] They have found a significant change in the magnetic properties of MnBi films due to Fe substitution. The out-of plane $M(H)$ hysteresis loops are almost rectangular for all the films, but the samples with higher Fe concentrations ($\geq 11\%$) show a signature of mixed phase. Figure 30 illustrates the room-temperature $M(H)$ loops of some selected samples, and the inset shows the loop of the sample with the highest Fe concentration of 16%, which suggests that the sample contains exchange-coupled hard and soft phases. It is believed that the Fe atoms that are not incorporated into the MnBi lattice have soft magnetic properties in these films. It is concluded that Fe doping has produced a significant change in the magnetic properties of the samples, including the decrease in saturation magnetization and magnetocrystalline anisotropy and the increase in coercivity. They explain these effects as the consequences of the competing ferromagnetic and antiferromagnetic exchange interactions of the interstitial atoms with the rest of the MnBi lattice.

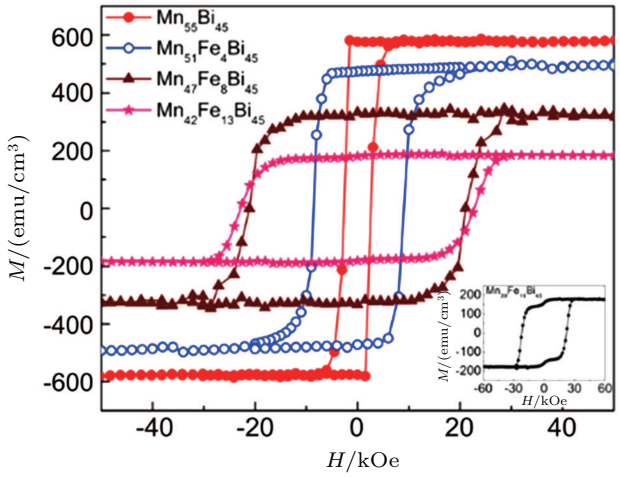


Fig. 30. (color online) The out-of-plane magnetization of $Mn_{55-x}Fe_xBi_{45}$ ($x = 0$, 4, 8, 13) films as a function of magnetic field measured at room temperature. The inset shows the room temperature M(H) loop of $Mn_{39}Fe_{16}Bi_{45}$ film.[93]

In fact, the investigations on the structural and magnetic properties of anisotropic MnBi films have been reported many times, but the exchange coupling on anisotropic MnBi/Fe films has been seldom reported. Figure 31 shows the depth profile by XPS study for MnBi/Fe film. It is found that MnBi/Fe film exhibits good multilayer structure. An Fe layer locates on the MnBi layer and the interface is rather sharp structurally.

No interfacial mixing presents because the Fe layer is sputtered at room temperature. It is also observed that the Mn element concentration slightly decreases as the etching position approaches the substrate, while the Bi element concentration increases. It is consistent with the XRD study that a few Bi atoms do not participate in the alloying process.[94]

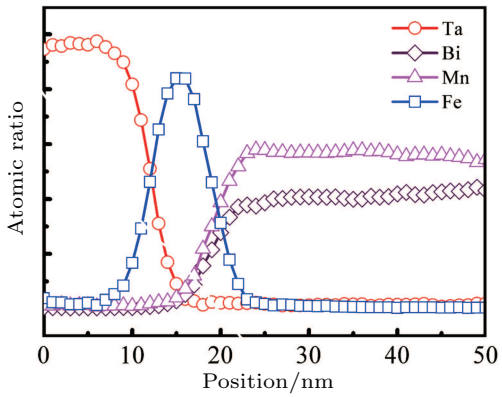


Fig. 31. (color online) The depth profile by XPS study for MnBi/Fe film.[94]

Figure 32 shows the out-of-plane hysteresis loops for MnBi/Fe nancomposite films at 300 K (black) and 400 K (red). The thickness of Fe layer is (a) 2 nm, (b) 4 nm, (c) 6 nm, and (d) 10 nm, respectively. When the thickness of Fe layer is less than 6 nm, the hysteresis loops at 300 K and 400 K show typical rigid magnet behavior with a single-phase-like reversal process, a smooth demagnetization curve, and a high magnetization squareness, indicating the effective exchange coupling between the hard and soft layers. The magnetization of the Fe layer is pinned in the direction of easy axis of the MnBi layer, leading to the behavior of coherent magnetization reversal. In comparison with a single MnBi layer, although H_C decreases considerably, M_R increases with the thickness of the Fe layer, exhibiting the effect of remanence enhancement. Accordingly, $(BH)_{max}$ improves from 7.6 MGOe to 8.0 MGOe at 300 K, and from 5.7 MGOe to 6.1 MGOe at 400 K, both of which exceed the largest reported values for MnBi magnets. As the thickness of Fe layer is 6 nm, rigid magnet behavior is maintained at 300 K. However, at 400 K, a pronounced step emerges on the demagnetization curve of MnBi/Fe film. The two-step reversal process, which is typical of the exchange spring behavior, originates from the decoupling of the soft Fe layer and the neighboring hard MnBi layer due to the decrease in the critical dimension for the soft phase and the increase in the anisotropy constant of the hard phase with increasing temperature. As the thickness of the Fe layer increases to 10 nm, both hysteresis loops show two-step reversal behavior at 300 K and 400 K. As a consequence, M_R/M_S and squareness significantly decrease.[94]

In summary, because the magnetocrystalline anisotropy of the ordered $L1_0$FePt phase is higher that of $Nd_2Fe_{14}B$, the effective exchange coupling length is shorter than that of the latter. In addition, the aligned FePt phase is generally formed on MgO substrate or crystalline layer at high temperature, thus, it is not suitable for designing an anisotropic hard/soft multilayer system.

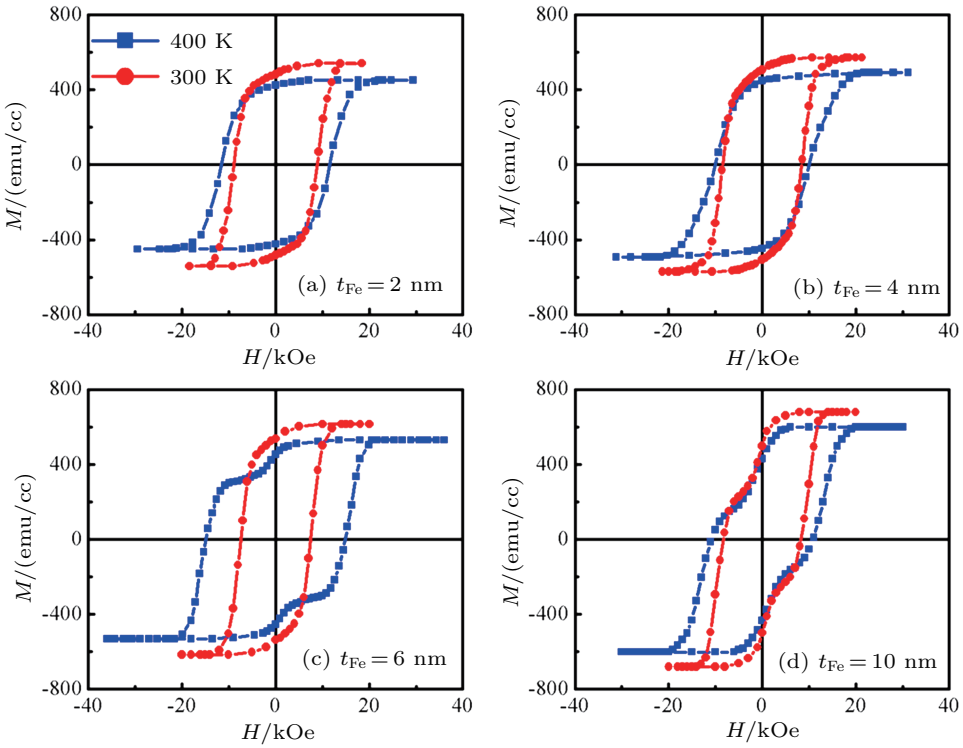


Fig. 32. (color online) Out-of-plane hysteresis loops for MnBi/Fe films at 400 K (square) and 300 K (circle). The thickness of Fe layer is (a) 2 nm, (b) 4 nm, (c) 6 nm, and (d) 10 nm, respectively.[94]

In anisotropic hard/soft magnetic multilayer films, a non-magnetic spacer layer is inserted in between the textured hard and soft-magnetic phase layers and the exchange-coupling interaction between the hard- and soft-magnetic phases is indirect and long-ranged. Thus, a new way is given to obtain a higher energy product in anisotropic nanocomposite hard/soft magnetic multilayer films. Some studies open a new discussion for comprehending the mechanism of long range soft- and hard-magnetic coupling in the anisotropic nanocomposite magnets. Predictably, if the method can be used in anisotropic nanocomposite magnets of a bulk system, it will play an important role in enhancing the magnetic properties of permanent magnet product in the future.

References

[1] Coehoorn R, de Mooij D B and de Waard C 1989 *J. Magn. Magn. Mater.* **80** 101
[2] Kneller E F and Hawig R 1991 *IEEE Trans. Magn.* **27** 3588
[3] Skomski R and Coey J M D 1993 *Phys. Rev. B* **48** 15812
[4] Ding J, McCormick P G and Street R 1993 *J. Magn. Magn. Mater.* **124** 1
[5] Manaf A, Buckley R A and Davies H A 1993 *J. Magn. Magn. Mater.* **128** 302
[6] Withanawasam L, Hurphy A S, Hadjipanayis G C and Krause R F 1994 *J. Appl. Phys.* **76** 7065
[7] Sun X K, Zhang J, Chu Y L, Liu W, Cui B Z and Zhang Z D 1999 *Appl. Phys. Lett.* **74** 1740
[8] Al-Omari A and Sellmyer D J 1995 *Phys. Rev. B* **52** 3441
[9] Liu J P, Liu Y, Skomski R and Sellmyer D J 1999 *IEEE Trans. Magn.* **35** 3241
[10] Shindo M, Ishizone M, Sakuma A, Kato H and Miyazaki T 1997 *J. Appl. Phys.* **81** 4444
[11] Liu W, Zhang Z D, Liu J P, Chen L J, He L L, Liu Y, Sun X K and Sellmyer D J 2002 *Adv. Mater.* **14** 1832
[12] Ao Q, Zhang W L and Wu J S 2006 *J. Magn. Magn. Mater.* **299** 440
[13] Zhang J, Takahashi Y K, Gopalan R and Hono K 2005 *Appl. Phys. Lett.* **86** 122509
[14] Liu W, Liu Y, Skomski R and Sellmyer D J 2006 *Handbook of Advanced Magnetic Materials* Vol. I, Chap. **6** p. 182 (New York: Springer)
[15] Liu W, Liu X H, Cui W B, Gong W J and Zhang Z D 2013 *Chin. Phys. B* **22** 027104
[16] Cui W B, Zheng S J, Liu W, Ma X L, Yang F, Yao Q, Zhao X G and Zhang Z D 2008 *J. Appl. Phys.* **104** 053903
[17] Cui W B, Liu W, Li J, Yang F, Zhang Q, Liu X G and Zhang Z D 2008 *J. Appl. Phys. D* **41** 245007
[18] Parkin S S P 1991 *Phys. Rev. Lett.* **66** 2152
[19] Gökemeijer N J, Ambrose T and Chien C L 1997 *Phys. Rev. Lett.* **79** 4270
[20] Cui W B, Liu W, Gong W J, Liu X H, Guo S, Yang F, Wang Z H and Zhang Z D 2012 *J. Appl. Phys.* **111** 07B503
[21] Hankel O 1964 *Phys. Stat. Solidi* **7** 919
[22] Cui W B, Takahashi Y K and Hono K 2012 *Adv. Mater.* **24** 6530
[23] Rodewald W, Wall B, Katter M and Uestuener K 2002 *IEEE Trans. Magn.* **38** 2955
[24] Lee D, Bauser S, Higgins A, Chen C, Liu S, Huang M Q, Peng Y G and Laughlin D E 2006 *J. Appl. Phys.* **99** 08B516
[25] Cui W B, Sepehri-Amin H, Takahashi Y K and Hono K 2015 *Acta Mater* **84** 405
[26] Kato H, Ishizone M, Miyazaki T, Koyama K, Nojiri H and Motokawa M 2001 *IEEE Trans. Magn.* **37** 2567
[27] Parkin S S, More N and Roche K P 1990 *Phys. Rev. Lett.* **64** 2304
[28] Slonczewski J C 1989 *Phys. Rev. B* **39** 6995
[29] Okuno S N and Inomata K 1994 *Phys. Rev. Lett.* **72** 1553
[30] Skomski R and Coey J M D 2016 *Scr. Mater.* **112** 3
[31] Dai Z M, Liu W, Zhao X T, Han Z, Kim D, Choi C J and Zhang Z D 2016 *J. Appl. Phys.* **120** 163906
[32] Bruno P 1994 *Phys. Rev. B* **49** 13231
[33] Bruno P and Chappert C 1991 *Phys. Rev. Lett.* **67** 1602
[34] Roy D, Sreenivasulu K V and Anil Kumar P S 2013 *Appl. Phys. Lett.* **103** 222406
[35] Davies J E, Hellwig O, Fullerton E E, Jiang J S, Bader S D, Zimanyi G T and Liu K 2005 *Appl. Phys. Lett.* **86** 262503
[36] Cornejo D R, Peixoto T R F, Reboh S, Fichtner P F P, de Franco V C, Villas-Boas V and Missell F P 2010 *J. Mater. Sci.* **45** 5077
[37] Hou H C, Kirby B J, Gao K Z and Lai C H 2013 *Appl. Phys. Lett.* **102** 162408
[38] Mayergoyz I D 1991 *Mathematical Models of Hysteresis* (New York: Springer)
[39] Pike C R, Roberts A P and Verosub K L 1999 *J. Appl. Phys.* **85** 6660
[40] Béron F, Ménard D and Yelon A 2008 *J. Appl. Phys.* **103** 07D908
[41] Pike C R, Ross C A, Scalettar R T and Zimanyi G 2005 *Phys. Rev. B* **71** 134407
[42] Muxworthy A, Heslop D and Williams W 2004 *Geophys. J. Int.* **158** 888
[43] Preisach F 1935 *Z. Phys.* **94** 277
[44] Néel L 1949 *Ann. Geophys.* **5** 99
[45] Winkhofer M, Dumas R K and Liu K 2008 *J. Appl. Phys.* **103** 07C518
[46] Yang C Y, Wang L W, Chen P A, Lin H J, Lai C H and Tseng Y C 2013 *J. Appl. Phys.* **114** 063902
[47] Gabay A M and Hajipanayis G C 2007 *J. Appl. Phys.* **101** 09K507
[48] Dai Z M, Liu W, Zhao X T, Wang T T, Li S K, Yu Y S, Zhao X G and Zhang Z D 2017 *Nanoscale* **9** 7385
[49] Ogawa D, Koike K and Kato H 2013 *J. Korean Phys. Soc* **63** 489
[50] Pike C R, Ross C A, Scalettar R T and Zimanyi G 2005 *Phys. Rev. B* **71** 134407
[51] Craik D J and Isaac E D 1960 *Proc. Phys. Soc* **76** 160
[52] Livingston J D 1985 *J. Appl. Phys* **57** 4137
[53] Hellwig O, Berger A and Fullerton E E 2007 *Phys. Rev. B* **75** 134416
[54] Hellwig O, Berger A, Kortright J B and Fullerton E E 2007 *J. Magn. Magn. Mater* **319** 13
[55] Bran C, Butenko A B, Kiselev N S, Wolff U, Schultz L, Hellwig O, Rössler U K, Bogdanov A N and Neu V 2009 *Phys. Rev. B* **79** 024430
[56] Neu V, Melcher S, Hannemann U, Fähler S and Schultz L 2004 *Phys. Rev. B* **70** 144418
[57] Kiselev N S, Dragunov I E, Neu V, Rößler U K and Bogdanov A N 2008 *J. Appl. Phys* **103** 043907
[58] Labrune M and Belliard L 1999 *Phys. Status Solidi A* **174** 483
[59] Lectard E, Allibert C H and Ballou R 1994 *J. Appl. Phys.* **75** 6277
[60] Kumar K 1988 *J. Appl. Phys.* **63** R13
[61] Fullerton E E, Jiang J S, Rehm C, Sowers C H, Bader S D, Patel J B and Wu X Z 1997 *Appl. Phys. Lett.* **71** 1579
[62] Prados C and Hadjipanayis G C 1999 *Appl. Phys. Lett.* **74** 430
[63] Zhou J, Kashyap A, Liu Y, Skomski R and Sellmyer D J 2004 *IEEE Trans. Magn.* **40** 2940
[64] Zhang J, Takahashi Y K, Gopalan R and Hono K 2007 *J. Magn. Magn. Mater.* **310** 1
[65] Fullerton E E, Sowers C H, Pearson J P, Bader S D, Wu X Z and Lederman D 1996 *Appl. Phys. Lett.* **69** 2438
[66] Singh A, Neu V, Faehler S, Nenkov K, Shultz L and Holzapfel B 2008 *Phys. Rev. B* **77** 104443
[67] Seifrt M, Neu V and Shultz L 2009 *Appl. Phys. Lett.* **94** 022501
[68] Al-Omari I A and Sellmyer D J 1995 *Phys. Rev. B* **52** 3441
[69] Yamazaki Y, Takano K, Takamura H, Sugimoto S, Homma M and Okada M 1998 *Mater. Trans. JIM* **39** 302
[70] Vlasko-Vlasov V K, Welp U, Jiang J S, Miller D J, Crabtree G W and Bader S D 2001 *Phys. Rev. Lett.* **86** 4386
[71] You C Y, Yang C, Zhang Z D, Han J S, Liu W and Sun X K 2003 *J. Phys. D: Appl. Phys.* **36** 423
[72] Choi Y, Jiang J S, Pearson J E, Bader S D and Liu J P 2007 *Appl. Phys. Lett.* **91** 022502
[73] Zhang J, Li Y X, Wang F, Shen B G and Sun J R 2010 *J. Appl. Phys.* **107** 043911
[74] Zhang J, Takahashi Y K, Gopalan R and Hono K 2005 *Appl. Phys. Lett.* **86** 122509

[75] Neu V, Häfner K, Patra A K and Schultz L 2006 *J. Phys. D: Appl. Phys.* **39** 5116
[76] Sawatzki S, Heller R, Mickel Ch, Seifert M, Schultz L and Neu V 2011 *J. Appl. Phys.* **109** 123922
[77] Leineweber T and Kronmüller H 1997 *J. Magn. Magn. Mater.* **176** 145
[78] Schrefl T, Forster H, Dittrich R, Suess D, Scholz W and Fidler J 2003 *J. Appl. Phys.* **93** 6489
[79] Asti G, Solzi M, Ghidini M and Neri F M 2004 *Phys. Rev. B* **69** 174401
[80] Pellicelli R, Solzi M, Neu V, Häfner K, Pernechele C and Ghidini M 2010 *Phys. Rev. B* **81** 184430
[81] Cui W B, Ma L, Sepehri-Amin H, Takahashi Y K and Hono K 2016 *Acta. Mater.* **107** 49
[82] Bruno P 1995 *Phys. Rev. B* **52** 411
[83] Thomas L, Kellock A J and Parkin S S P 2000 *J. Appl. Phys.* **87** 5061
[84] Akdogan O, Sepehri-Amin H, Dempsey N M, Ohkubo T, Hono K, Gutfleisch O, Schrefl T and Givord D 2015 *Adv. Electron. Mater.* **1** 1500009
[85] Liu J P, Luo C P, Liu Y and Sellmyer D J 1998 *Appl. Phys. Lett.* **72** 483
[86] Jiang J H, Tezuka N and Inomata K 2006 *J. Magn. Magn. Mater.* **302** 40
[87] Liu Y, George T A, Skomski R and Sellmyer D J 2011 *Appl. Phys. Lett.* **99** 172504
[88] Heikes R R 1955 *Phys. Rev.* **99** 446
[89] Chen T 1974 *J. Appl. Phys.* **45** 2358
[90] Chen T and Stutius W 1974 *IEEE Trans. Magn.* **10** 581
[91] Guo X, Chen X, Altounian Z and Ström-Olsen J O 1992 *Phys. Rev. B* **46** 14578
[92] Cao S, Yue M, Yang Y X, Zhang D T, Liu W Q, Zhang J X, Guo Z H and Li W 2011 *J. Appl. Phys.* **109** 07A740
[93] Kharel P, Li X Z, Shah V R, Al-Aqtash N, Tarawneh K, Sabirianov R F, Skomski R and Sellmyer D J 2012 *J. Appl. Phys.* **111** 07E326
[94] Li B, Liu W, Zhao X G, Gong WJ, Zhao X T, Wang H L, Kim D, Choi C J and Zhang Z D 2014 *J. Magn. Magn. Mater* **372** 12